POLITECNICO DI TORINO

Dipartimento di Elettronica e Telecomunicazioni

Corso di Laurea in Nanotechnology for the ICT's

Tesi di Laurea Magistrale

Monolithic InAs/InGaAs quantum dot lasers

Experimental sub-threshold characterization of single section, broad-area devices for different *p-doping* concentrations and active region lengths

Relatore
Prof. Paolo Bardella

Correlatore:
PD Dr. Stefan Breuer

Laureando
Matteo Angelozzi

Anno accademico 2018/2019

Summary

Monolithic mode-locked edge-emitting semiconductor quantum dot lasers emitting at 1.26 μm are ideal sources for the generation of optical frequency combs for short-reach inter- and intra-data center links.
The modal dispersion and gain properties determine their suitability for ultra short optical pulse generation by mode-locking. In this elaborate, as a first step, the power vs. current characteristic, the modal gain and the dispersion properties on $InAs/InGaAs$ *single section* quantum dot lasers with a 50 μm broad-ridge waveguide are experimentally investigated. This analysis focuses on spectrally-resolved gain, temperature dependence and near field investigation, trying to highlight the influences of the different p-doping values, different active region lengths and broad area effects.

In Chapter 1 introductory matter is discussed, a brief summary of the technological motivation which led us to the modern state of the art on QD laser and a further motivation on why this is an hot topic, are given. Moreover, an general overview on how these devices are modelled is provided.
In Chapter 2 the description of how the experimental characterization was carried out and insights on the various setups used, within the technical motivation, are shown.
In Chapter 3 the elaborate will focus on the analysis of the obtained results as well as considerations about them. The post-processing methods used are widely described and segments of scripts, created ad-hoc, are shown.
Due to the large number of data, all the detailed plots and graphs inherent to the post-process are stored in Appendix A, whereas in the main chapters they are summarized in more general and explanatory plot.
In Appendix B a compact version of the script used for several simulation are reported.

Acknowledgements

I would like to acknowledge professor Wolfgang Elsäßer, Stefan Breuer, Chistoph Weber, Dominik Auth and every single member from the albleiteroptik team of the Thechnische Universität Darmstadt, for make this thesis possible by means of involving me in the project, providing me the instruments and the laboratory access, but most importantly, for providing me strong support with their kindness.

To all my friends, who traveled with me all along this journey,
through good times and bad times.

To Elena, who makes me want to be the best version of myself, everyday.

To my father and my mother, for believing in me, always.

Contents

List of Figures

Chapter 1

Introduction

1.1 History

In 1917, Albert Einstein wrote the theoretical basis for the *light amplification by stimulated emission of radiation* in the paper "On the Quantum Theory of Radiation" by means of derivation of Max Planck's law, introducing probability coefficients aimed to describe the absorption, spontaneous and stimulated emission.
We have to wait almost fifty years before the very first laser appears, in 1960 Theodore H. Maiman at Huges Research Laboratories built the first solid-state laser based on a synthetic crystal of ruby, pumped by a flash lamp and emitting at 694 nm [1]. On the other hand, the concept of emission through carrier recombination in a p-n junction, was introduced by Basov [2] in the 1958, and two years later the first semiconductor based laser emitting in the visible range was built.
At that time, the knowledge on semiconductors photonic was limited to the Silicon, which is an indirect bandgap semiconductor and therefore not suitable for recombination processes; the concept of using a III-V heterojunction was already taken into account but we have to wait until the 1962 when at the MIT Lincoln Laboratory [3] the radiation from carrier recombination were created in GaAs junction at cryogenic temperature. From there on, several research groups started to individually develop heterostructure diode lasers. In 1970, at Bell Company, Izuo Hayashi and Morton Panish [4] developed the first semiconductor laser, based on a heterojunction, working at room temperature and in continuous wave regime, but the manufacturing processes, as well as manipulation methods, for compound semiconductor were not totally handled and the progress in semiconductor optic was slow.
In the last half of the 20^{th} century the semiconductor industry started a fast growth, the material science progress and the new technologies for fabrication and manipulation opened the doors to a wide field of opportunities which led the word into the microelectronic era. Side by side the electronic, also the interest in the semiconductor optic started to arise, new deposition techniques allowed the creation of heterostructure based on different materials, overcoming limitations and allowing the increment of the integration density. The better comprehension of the physics behind the electronic structure led to the so called bandgap engineering, giving the chance to tune the devices in wavelength suitable for different applications.

1.2 State of the art

Nowadays the technological processes and the deeper knowledge of the electronic structure of semiconductors give us the opportunity to work at the quantum level by means of spatial confinements of carriers, in one (*quantum wires*), two (*quantum wells*) and three (*quantum dots*) dimensions. The confinement of electrons and holes has, as a consequence, the variation of their density of states, which directly alters the generation/recombination process, the further the confinement the higher the density of states for low energy.
In this elaborate the focus will be on Quantum Dot (QD) lasers, in which the three dimension confinement of the carriers should result in a delta-like density of states, but due to process variation, the dots sizes undergo a statistical variation and this, jointly with the dots shape, causes the delta-function density of states to broad into a gaussian-like DOS.
The realization of QDs with characteristic dimensions significantly smaller than the De Broglie wavelength, has been possible thanks to the continuous development of advanced epitaxial growth techniques such as Molecular Beam Epitaxy (MBE) and Metal Organic Vapour Phase Epitaxy (MOVPE) techniques. III-V QDs can be grown by MBE exploiting a self-assembling technique called Stranski-Krastanov (SK) growth method. This technique is essentially a controlled evaporation from various elemental sources in high vacuum onto a temperature-controlled single crystal substrate. The idea of epitaxy is that in the growing layer, the newly arriving atoms incorporate at the precise positions established by the immediately preceding atomic layer. Generally, in such processes, a complete lattice matching or a small lattice mismatch between the grown material and the substrate must be preserved. However, if the difference between the lattice constants (a) of the two materials exceeds a certain critical value (typically $\Delta a/a \geq 1\%$), under particular growth conditions, islands formation via the so called Stranski-Krastanov (SK) process can be obtained. A more detailed treatment of this process can be found at [7].
The SK process involves therefore the growth of highly lattice mismatched materials e.g. InAs on a GaAs substrate $\Delta a/a = 7\%$. In this case, during the initial stage of deposition, the in-plane lattice parameter of the InAs tends to match that of the GaAs substrate, forming a thin strained layer that is usually called wetting layer (WL). When the amount of deposited InAs exceeds a certain critical value (typically 1-2 monolayers), strain relaxation leads to the formation of islands. This process is due to the relaxation of the elastic energy induced by the lattice mismatch and occurs without the formation of dislocations. This process widely depends on the growth parameters such as growth temperature, deposition rate and amount of deposited material, influencing therefore the QD density, size and shape.

This is the reason for the statistic nature of the quantum dot ensembles, both size and position are stochastic, leading to the above mentioned consequence. Nevertheless this homogeneous broadening does not affect the predicted improvements of QD lasers with respect quantum well active region laser.
In the static characterization scenario, higher net modal gain, higher optical power, lower threshold [5], less sensitivity to operating temperature [6] and a near-zero linewidth enhancement factor have been theoretically modelled and experimentally verified in the past years.
Further improvements have been achieved by the application of p-doping on the wetting layer above the quantum dot one: valence states in quantum dot's potential well are closer in energy with respect to the conductive ones due to the higher hole's mass in the III-V semiconductors, this leads to an asymmetry in the quasi-Fermi levels movement, hence higher carrier density needed to achieve the transparency threshold. Even tough the presence of dopant could increase the non-radiative recombination and could bring unwanted increase on internal loss, in quantum dot lasers the low number of actually active states require a low level of doping, therefore non of the above mentioned issues should arise.
Nowadays, the increasing requirement of bandwidth due to the improvements achieved in the high data rate wireless networks, opens the way to the research on the high-frequencies, which would provide the requested bandwidth. In this frame, due to the lack of technology in the electronic side, the optical integration for THz and sub-THz generation became of strong interest. Systems based on photomixing and receivers based on optical heterodyning allow very high speed data modulation and bit rate modulation [15].
Talking of semiconductor lasers under optical injection regime, several ways of creating *optical frequency combs* are being intensively investigated in the last years, the comprehension of such behaviour requires a deep investigation and characterization of the fundamental physical operations of new kind of semiconductor laser, such as sub-threshold behaviour.

1.3 Case of study

Semiconductor heterostructures under examination are monolithic, single section devices, with facet as cleaved. Ten layers of InAs/InGaAs Quantum Dot separated by a GaAs wetting layer and with 50 µm active region width with three different levels of wetting layer p-doping, $5 \times 10^{17}\text{cm}^{-3}$, $3 \times 10^{17}\text{cm}^{-3}$ and undoped. Moreover, for each doping concentration there are four active region length, 2 mm, 1.5 mm, 1 mm and 0.6 mm respectively, each one of these 12 devices has two nominally identical copies, for a total of 36 devices.
The focus of this elaborate is the sub-threshold characterization by investigating the relation of fundamental parameters with p-doping modulation and active region length variation. Moreover, the large value of the active region width needs to be carefully treated because of higher order lateral modes guided.

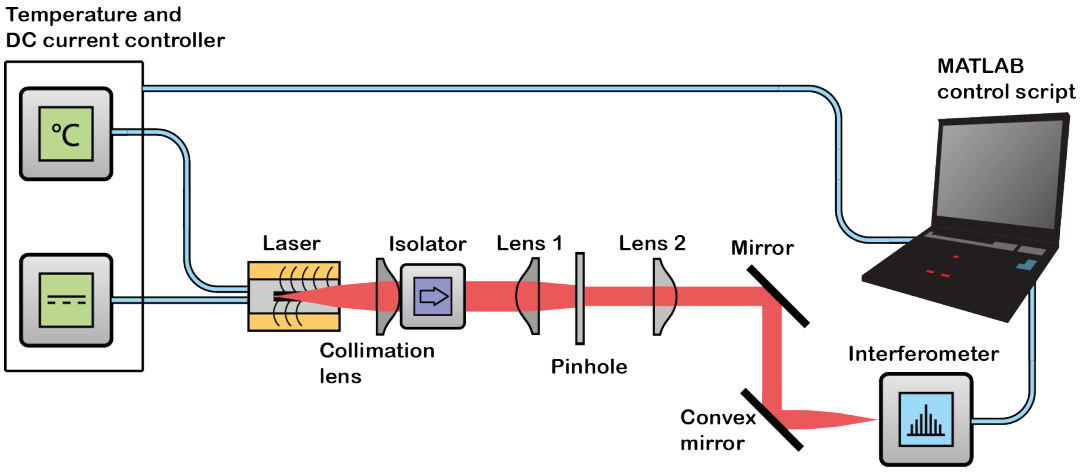

Figure 1.1: Experimental filtering setup for high order mode and measurements.

The characterization was carried always in continuous current injection regime, the use of a pulsed injection was taken into account to avoid a possible heating of the devices, but in the range of injection currents no overheating occurs.
Most of the measurements was taken under controlled temperature of 25°C and in free space. During some characterizations the use of single mode fiber was needed, but, due to the multi-modal nature of the emission, the major issues were related to the severe power losses.

This work is part of a bigger picture involving three different universities and their research team. The research is still ongoing on different level of characterization and preliminary results are being presented in conferences [16, 17, 18].

1.4 Theory of Quantum Dots

1.4.1 Electronic properties

For the purpose of this thesis is useful to briefly discuss about what concern QD based active region. the characteristic confinement potential can affect the wavefunctions, energy levels and interband transitions energies in self assembled QDs. In order to describe the electronic properties of the semiconductor QDs we need at first to compute the electron and hole single-particle eigenstates. Self-assembled QDs described in the previous section are mesoscopic structures i.e. the QD dimensions are significantly larger than the unit cell of the semiconductor material. In this case the effective mass approximation can be safely adopted to compute the single particle eigenstates. Electron and hole wavefunctions $\Psi_\lambda(\vec{r})$, where $\lambda = e/h$ is the band index, can therefore be written as follows:

$$\Psi_\lambda(\vec{r}) = \varphi_\lambda(\vec{r})\, u_\lambda(\vec{k} \simeq 0, \vec{r}) \tag{1.1}$$

$\varphi_\lambda(\vec{r})$ are slowly varying envelope functions whereas $u_\lambda(\vec{k} \simeq 0, \vec{r})$ are the Bloch function evaluated close to the band edge $\vec{k} \simeq 0$. Within a parabolic band approximation, the envelope functions satisfy the effective mass equation:

$$\left(-\frac{\hbar^2}{2m^*_\lambda}\nabla^2 + V_\lambda(\vec{r})\right)\varphi_\lambda(\vec{r}) = \varepsilon_\lambda \varphi_\lambda(\vec{r}) \tag{1.2}$$

where m^*_λ is the effective mass and $\hbar$ is the Plank's constant divided by 2π. $V_\lambda(\vec{r})$ is the 3D QD confinement potential for electron and holes. In [8], the QD was considered as a 3D box with infinitely high potential wells. In [9], it was shown that wavefunctions in lens shaped QDs having radius significantly larger than the QD height, can be well approximated by those of a 2D harmonic potential along the in-plane directions (y,z) (weak confinement) and of a strongly confined potential well along the growth direction (x).
The solution of this work-frame implies the change to cylindrical coordinates which led to transverse and in-plane wavefunction, which mathematical solution is out of the purpose of the thesis. Due to the assumed confinement potential, the solution of the physical model yields an infinite set of equally spaced confined electron and holes energy levels. It must be pointed out however that this picture completely fails in describing high energy QD states. In real QD systems, due to the finite confinement potential, the energy levels tend to become closely spaced and highly degenerate at high energies, due to a weaker localization of the high order eigenfunctions. Furthermore, in real QD systems, hole wavefunctions are weakly confined if compared to electron wavefunctions in conduction band. The spacing between confined energy levels for holes in the valence band is therefore much smaller than that for the electrons.

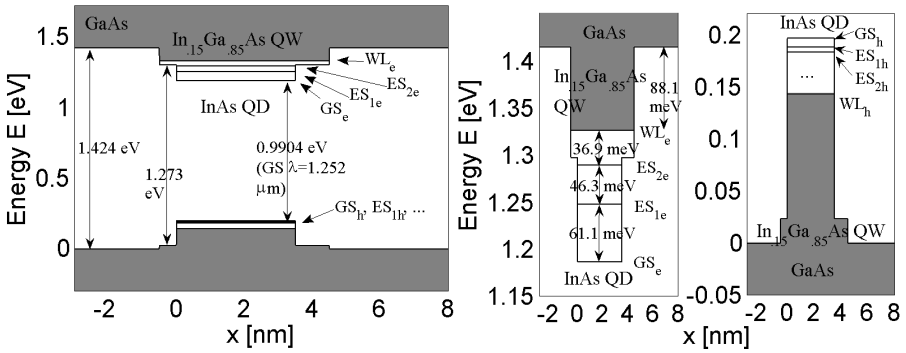

(a) (b)

Figure 1.2: (a) Schematics of the energy band structure for a InAs/GaAs DWELL layer; (b) Characteristics intraband and interband transition energies are reported.

Furthermore in the valence band, due to the large heavy hole (HH) effective mass, 2D WL/QW delocalized states are much closer in energy to the QD confined energy levels.
As an example of this complex picture, in figure 1.2 the schematic band structure for an InGaAs/InAs heterostructure with intra/inter-band transition are depicted. The InAs/InGaAs DWELL layer energy level diagram is consistent with those reported in [10, 11, 12].

1.4.2 Optical properties

In this section we give a basic description of the optical properties of self assembled QDs. Equations governing population and polarization dynamics within the QD confined states are presented and expressions for the QD optical susceptibility and the power spectral density of the QD spontaneous emission noise are reported.
Let consider therefore an ensemble of self assembled QDs. As pointed out in Section 1.4.1, QDs can have different size, composition and shape leading to different characteristic interband transition energies. In the following treatment, we subdivide therefore the QD ensemble in N groups (with N odd) according to their characteristic GS interband transition energy. QDs belonging to the same group are supposed to be identical. The probability that a QD belongs to a certain group with a given GS interband transition energy $\hbar\omega_{i,GS}$, with $i = 1...N$, is assumed to follow a Gaussian distribution:

$$G_i = 1/Z \exp\left(-4\log 2 \frac{\hbar\omega_{i,GS} - \hbar\omega_{(N+1)/2,GS}}{\Delta E^2}\right) \tag{1.3}$$

where Z is a normalization constant such that $\sum_i G_i = 1$ and ΔE (in eV) is the Full Width at Half Maximum (FWHM) of the Gaussian distribution. Each

QD group will therefore contribute in a different way to the optical macroscopic polarization.
Under this assumption, one can evaluates the response of each QD group to an external electromagnetic field through the density-matrix theory, whose main advantage is to allows the introduction of phenomenological scattering rates during the derivation. The mathematical approach is complex and out of the purpose of this elaborate.

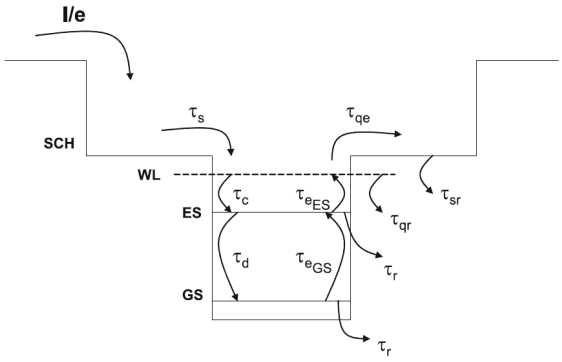

Figure 1.3: Band diagram for a single dot system. Rates are also depicted.

This approach leads to the model that is used for the simulation of the static dynamic characteristics of a QD laser, the *multi-population rate equation model*. For the simulation of a single QD several parameter has to be involved into the model: a first well state, from where the injection takes place, the wetting layer state acting as a carrier reservoir and then the dot state, which must be coupled to the wetting layer and must represent also the inhomogeneity due to the dot size distribution.
Under several assumption such as

- only two state for the, dot GS and ES (ground state and excited state);
- only electrons dynamic considered (holes are "lighter" and they will follow the electron dynamics);
- the fluctuation in size of the dots is taken into account using equation 1.3;
- stimulated emission can take place only for recombination in excited and ground states.

all the capture times, from the barrier to the wetting layer, from wetting layer to excited state and from excited to the ground state; as well as all the escape time, from ground to excited state, from excited state to wetting layer and from wetting layer to the barrier, are introduced in the model. The recombination rates, both radiative and non-radiative, from every state in the system complete the model. A summary of this model is depicted in figure 1.3 [13].

Chapter 2

Measurements set-up

In the following chapter, the schemes of the experimental setup and a brief description of the equipment will be provided.
The whole characterization is carried in DC injection current regime, at $25°C$. The use of a pulsed injection can be taken into account for avoiding the overheating of the devices, which would result in a direct effect on the carrier population, but only for temperature far above the value chosen in this characterization, in this range the DC injection does not lead to any temperature issues.
Some slightly different operation conditions are used for measurements such as temperature sensitivity characterization or the imaging of the beam profile, but they will be specified case by case later.

All the setup have in common the control unity for the current injection and the block temperature. All the lasers are provided with the active region already wired for a simpler bias configuration, avoiding the use of needles in direct contact with the devices. Moreover, being the whole set of devices "single section", the only bias provided is the injection current.

2.1 Power measurement

The very first required step was the measurement of the optical output power by means of a photodetector. The used method is the simple detection of the stimulated emission, propagating in free space.
The beam is focused, through a collimation lens, into the detector aperture. Since the maximum detectable power is 10mW, the use of an attenuator was needed. Moreover, in order to avoid unwanted reflection an isolation unit was interposed between the collimation pack and the photodetector.

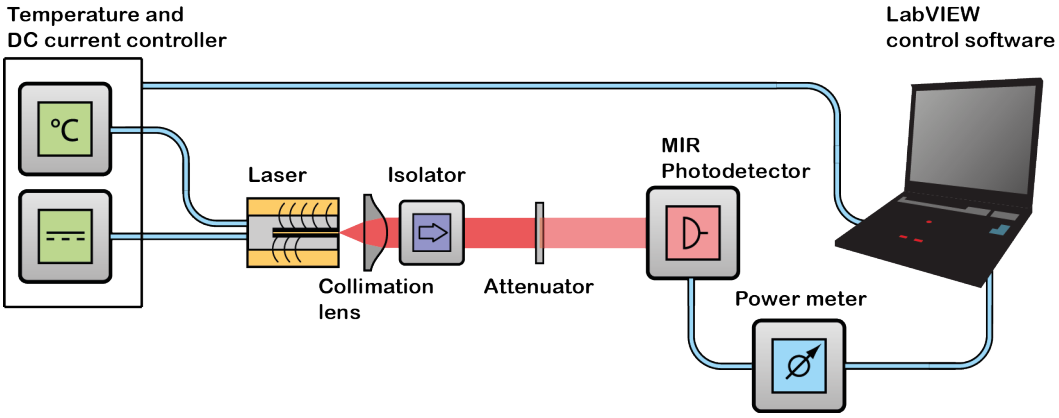

Figure 2.1: Experimental setup for power measurements.

The scheme of the setup is shown in figure 2.1. The Control unity is used to keep the temperature constant through a PID control loop setted with the correct value for the cooling block in use.
The DC injection is also set by the control unity and the feedback loop received from the LabVIEW script, which is responsible for the acquisition of the data and the increasing and decreasing of the bias current by means of stepping chosen a-priori.
Once the setup is built, the operator must provide the maximum input power at the detector by optimizing the beam alignment before starting the measurement. The signal detected by the photodetector is visualized on a digital power meter, which perform an average on several signal detected. Then the digitalized detected value is sent to the control software which perform the final measurement and send the increase/decrease signal to the DC current control in order to obtain the full spectra.
Talking about optical power output, is useful to perform a double check of the P-I characteristic, first going toward higher value, from ~ 0 mA to 900 mA, then from higher to lower values. This allow to detect eventual hysteresis cycle in the nearby of the lasing threshold.

2.2 ASE and interferogram measurement

Concerning the measurement of the amplified spontaneous emission, the experimental setup has the same basis. The control unit for DC injection and temperature is the same as the one described in the previous case, the beam exiting from the laser facet is collimated through a lens, isolated from eventual optical reflection and then aligned inside the interferometer.
The alignment line needs a 45 ° mirror, the beam needs to be direct onto a convex mirror which further collimates the beam before the FTIR interferometer.
FTIR stands for Fourier-Transform Infrared Spectroscopy, technique which is usually used for study the infrared footprint of a given sample. In this case it turns out to be a solid and reliable technique for the characterization of the semiconductor laser emission spectra. Thanks to its rapid measurements allows to avoid any fluctuation in the spectra that can be caused by temperature or current variation, moreover, the wavenumber scale is precisely obtained from an external $HeNe$ solid state laser at 633 nm.

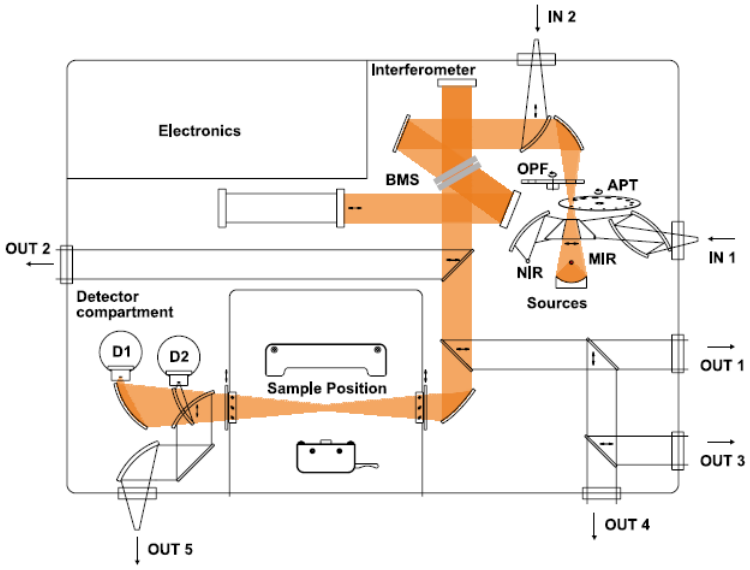

Figure 2.2: Internal scheme of FTIR interferometer VERTEX 80v from Bruker.

Beside the alignment line, the main part of this setup is the interferometer. The one provided in the laboratory is the VERTEX 80v, an advanced optical bench equipped with an high resolution interferometer which cover a wide spectral range. In figure 2.2 the beam path inside the VERTEX is shown, in our setup the pre-aligned beam is focused inside the *IN 1* where it enters inside a classical Michelson interferometer configuration. The instrumentation is equipped with different beam-splitter, one for different range of wavelength; in the near-infrared the CaF_2 based beamsplitter is needed.

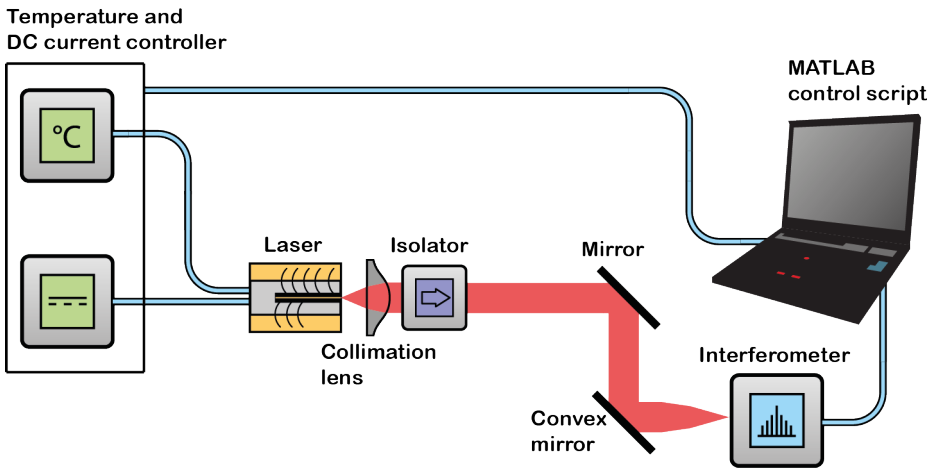

Figure 2.3: Experimental setup for ASE and interferogram measurements.

The laser emission enters, replacing the NIR source. An important point to be remarked is that the throughput of such interferometer depends on the diameter of the collimated output of the laser, this is because convergent rays are modulated at different frequencies as the path difference is varied. Therefore, for a given resolution and wavelength this circular aperture allows more light through than a slit, resulting in a higher signal-to-noise ratio. [14]

2.2.1 Far-field measurement

The method used for filtering everything but the central mode consist in the re-imaging of the lateral far-field at the back of the focal plane of the collimation pack, through the 10 μm pinhole. The pinhole filter out the high order lateral modes, then the fundamental emission should be aligned inside the interferometer setup for the detection of ASE and interferogram spectra.

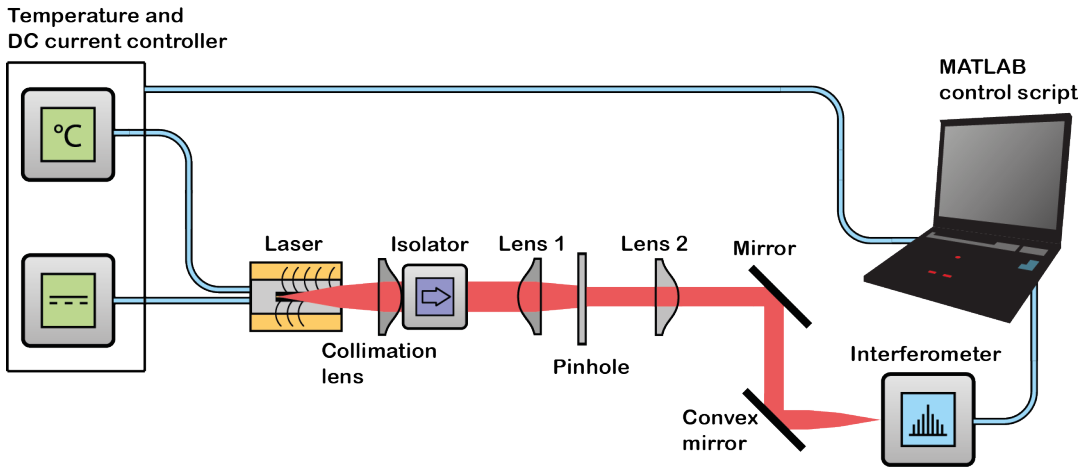

Figure 2.4: Experimental filtering setup for high order mode and measurements.

The ensemble of re-imaging lens, pinhole and relay lens is the critical point of this setup, the alignment of the central mode inside the pinhole is not straightforward at all, both the lens 1 and 2 in 2.4 were both located on two different three-axis controlled mounts, then the alignment procedure was carried out by maximizing the output power at the back of the pinhole by means of a power meter (similar setup of 2.1). Also the selection of the correct aperture of the pinhole required several trial.

Is also useful to mention that, before the final setup in figure 2.4, another experimental solution was tried out. The idea was to select only the central mode by coupling the laser emission into a single mode fiber, whose output would be directly aligned inside the interferometer. This solution had to be discarded because of its high power losses, in fact is important to remember that the measurements to be performed are measurements below threshold, and this implies a very low available output power which could lead to high noise errors in the ASE spectra detection. Through the Matlab script it is possible to select the step in the current injection, the settings for the data collection and several other features, while the dedicated software (OPUS Spectroscopy Software) allows the selection of parameters such as wavelength resolution, scanning time, number of scan for each measurements etc.

2.3 Near field measurement

In order to verify experimentally that the the filling of the ASE spectra valleys is a direct consequence of the high order modes guided by the wide active region, is necessary to investigate the beam profile. The filling of the ASE spectra is the phenomenon for which the maximum to minimum ratio to be lower than the fundamental mode ASE alone [30].
The study of the near-field emission is carried out in two different ways, one involve the direct imaging of the beam through the use of a CCD camera, working in the near-infrared region, then, a fiber-scanning technique is implemented in order to obtain a more precisely evaluation of the beam profile.

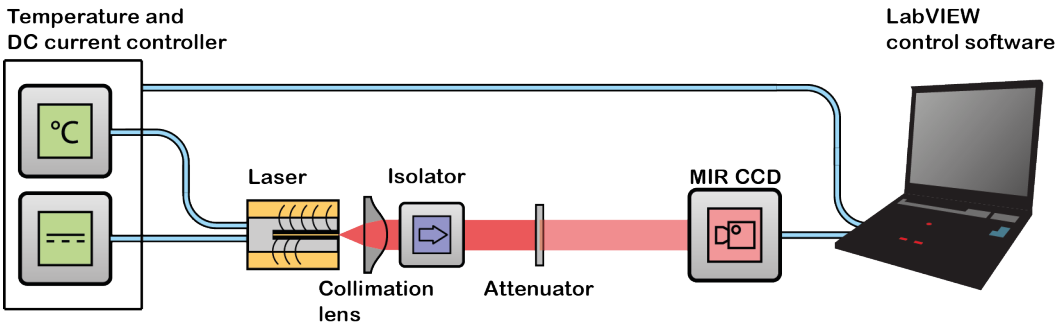

Figure 2.5: Experimental setup for near-field imaging.

The experimental setup for the CCD imaging is similar to the setup used for the measurement of the output optical power in figure 2.1. Also in this case, since the CCD camera input cannot be greater than 10 mW, an optical attenuator is needed after the collimation pack. The CCD output is directly connected to a monitor which allows to tune the sensibility and the response of the camera to the input signal. Then the acquisition process is managed by an ad-hoc LabVIEW software from which the number of acquisition point, number of measures to be averaged and acquisition time. The full datasets are then saved in bidimensional matrix which will be post-processed in order to obtain an imaged map of the beam in the near field.

The imaging technique above has the benefit to provide a 3D map of the field, but on the other hand it has low resolution and can only give the general shape. The setup used for distinguish the contribute of high order modes is the one depicted in figure 2.6. The laser emission is directly coupled inside a multimodal optical fiber, then the output is scanned directly in front of NIR photodetector/power-meter ensemble to measure point-by-point the optical power.
The critical point of this setup is the automatism, which is responsible for the fiber output scan. From the previous setup 2.5 we are able to discern the major axis of

emission, i.e. the axis along which the high order mode contributes to the beam profile, therefore is important to be able move the fiber in a 2D grid in order to optimizing the acquisition of the profile.

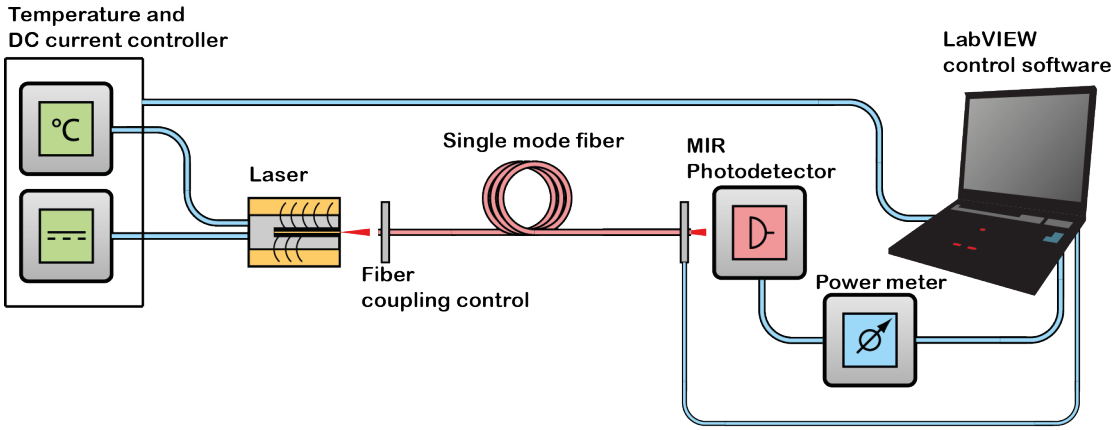

Figure 2.6: Experimental setup for near-field profile measurement.

The automatism is composed by two stepper motors which gives 2 degree of freedom to the end of fiber in the plane parallel to the photodetector. Before start the measurements, through the use of a power meter, the optical power at the detector input is maximized, both along x and y axis, if this step is performed correctly, that will correspond to the central peak of the multi-mode profile.
Then, the starting point of the measurements is chosen to be shifted, along the major axis emission, in order to get the whole profile within a single scan. All the setup is supervised by a central unit of control, by means of a LabVIEW script is possible to tune the number of acquisition point, the stepping distance an the time for each measurement.

Chapter 3

Post-process analysis

For the sake of clarity, due to the large number of analysed data, in here only some plots will be reported. Depending on the parameters in analysis and on the information considered to be more relevant, a comparison will be shown between devices with same doping level but different active region length or identical device with p-doping modulation.
All the post-processed data plots will be reported in the Appendix A.
From now on, for clarity of notation, devices with different p-doping concentration value will be labelled as:

- **Group A**: undoped;
- **Group B**: $3 \times 10^{17}\, cm^{-3}$ p-doped;
- **Group C**: $5 \times 10^{17}\, cm^{-3}$ p-doped.

3.1 P-I curves

The acquisition of the optical output power gives many information such as power range and threshold current values, from which the evaluation of the wall plug efficiency (WPE), the quantum internal efficiency and eventually the differential resistance can be carried out.

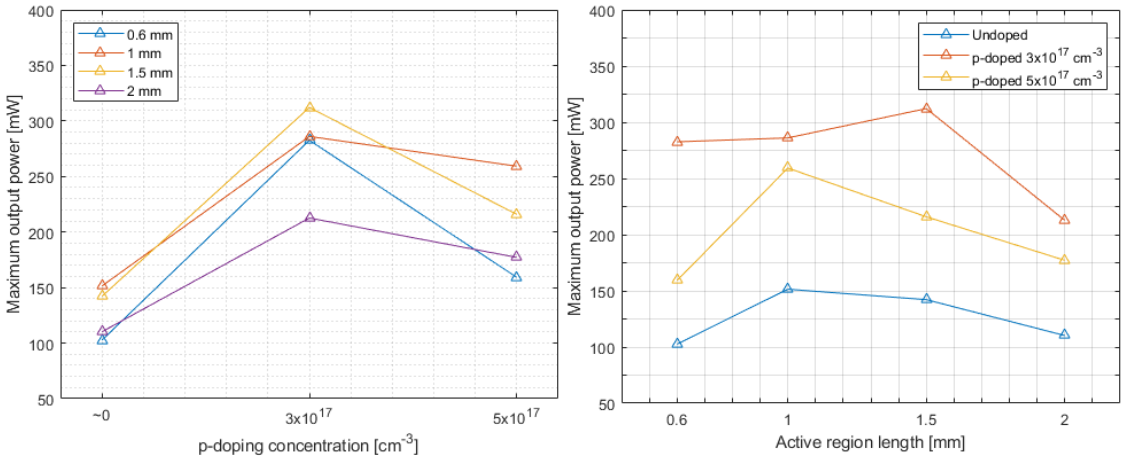

(a) p-doping modulation

(b) Active region length modulation

Figure 3.1: Optical output power values at 950 mA.

The complete dataset of P-I curves can be found in Appendix A, as well as the WPE plots. In here we will describe the most noticeable informations extrapolated from the measurements, trying to depict the situation by focusing on the effects of doping and active region length modulation.
The whole set of devices is investigated in the range of injected current from 0 up to 950 mA, at controlled operation temperature fixed at 25 °C.
Of course, since we are dealing with different active region length, is important to consider the density of injected current in order to have a common reference. For this reason, the range of injected current is not the same for every sample, but since the main purpose of this research is the sub-threshold characterization, the discrepancy of range does not bring any issue.
In figure 3.1 can be notice the behaviour of the optical power at 950 mA, sub-figure (a) shows the maximum optical power as a function of p-doping level, for the different investigated device length. The trend for each active region length is clearly the same and is evident the strong increase of power between group A and group B. For every length, the power almost rises up until twice the original value, which is an increase of the 100 %.

Then, for the group C it seems like the amount of optical power starts to decrease, but it is important to remark that this assumption is supported by the mere P-I curve. As we can see in figure A.1 in every sub-figure, a part for the 0.6 mm set, for every device the saturation is not reached. Thus, one cannot state that the optimal device set for max output power is group B.
For what concerns the effect of the active region length, in figure 3.1 (b) the maximum optical output power, at a cooling block temperature of 25 °C and with an injection current of 950 mA, is depicted as a function of active region length for different doping concentrations; there is no evidence of a general trend, the 1.0 mm and 1.5 mm devices seems to have a slightly more optical power, but the ΔP is always lower than $\sim$ 100 mW

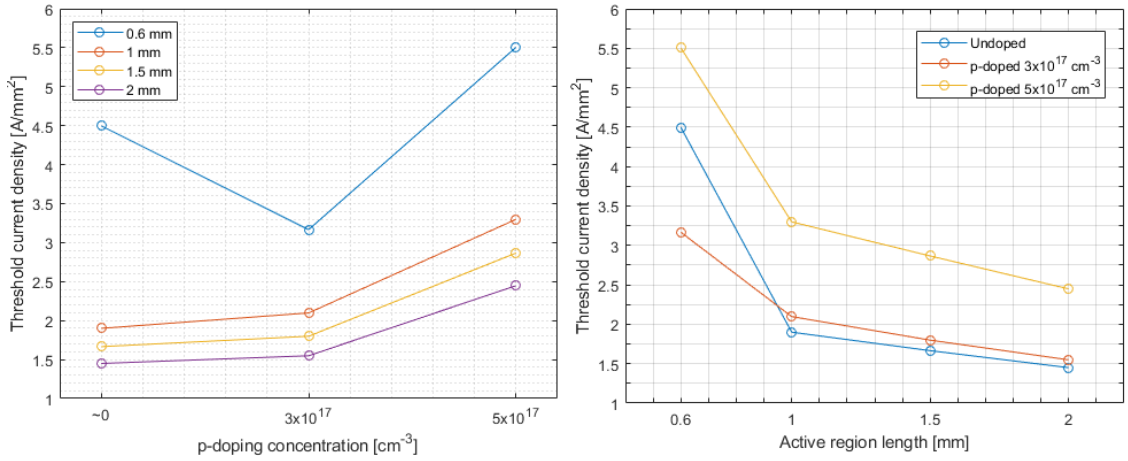

(a) p-doping modulation

(b) Active region length modulation

Figure 3.2: Threshold current densities.

Very interesting are the results regarding the threshold current values shown in figure 3.2: for different doping concentration (a) and different active region lengths (b). The values are shown in terms of current density in order to have a common reference for every device.
The behaviour is very clear, as the active region length increases the threshold goes toward lower values, the effect of the device length is strong, shorter devices show a much higher threshold with respect to the longest, and also if we have seen that the longer lasers tends to have a low output power, the advantages of having such a lower threshold must be taken into account.
In table 3.1 the threshold values are provided in mA aside the corresponding maximum power measured at 950 mA.

3.1.1 Wall Plug Efficiency

The wall plug efficiency is defined as:

$$WPE = \frac{P_{out}}{P_{el}} \tag{3.1}$$

This value can be seen as a measure of how much the device is efficient to convert the electrical into optical power. Therefore P_{el} is evaluated knowing a priori the value of the differential internal resistance of the device, which is extrapolated automatically from the current control unit.
The WPE behaviour for the full set of devices can be found in Appendix A.2, here is the summary of the obtained results.
From figure 3.3, it is easy to notice how the largest values of efficiency can be obtained from the devices group B, in particular from the 1.5 mm long one.
Moreover, the undoped devices show in general the worst values, always under 10 % and, as for the power, no particular effects of active region length is found.

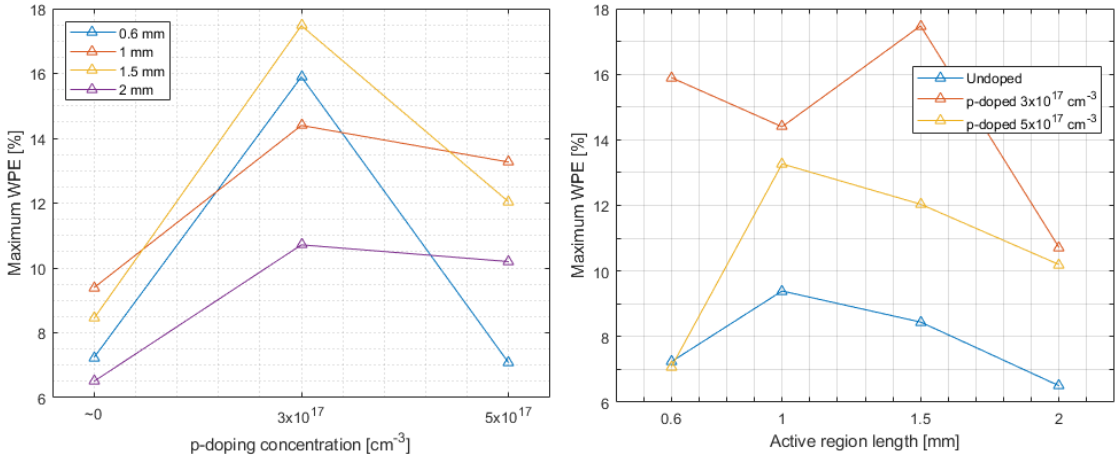

(a) p-doping modulation

(b) Active region length modulation

Figure 3.3: Maximum wall plug efficiency.

Again, it is important to remark that these values are taken in a given range of input current in which almost no device reached the saturation, therefore all the consideration regarding power and WPE made so far, have to be taken as mere speculation of what can be the overall behaviour of every devices pushed into saturation. As a matter of fact is already known that for higher current value, the first excited state of the quantum dots starts to make its contribution to the emission [16] [17].

An interesting speculation can be carried out if one considers that the output optical power can be written a

$$P_{out} = \eta_d \frac{\hbar\omega}{q}(I - I_{th}) \tag{3.2}$$

where η_d is the differential quantum efficiency.
It is easy to see how, starting from the slopes of the P-I characteristics in figures A.1, it is possible to evaluate the differential quantum efficiency point by point. Moreover, by using an empirical model for the description of the carrier behaviour inside the active region, η_d can be written as

$$\eta_d = \eta_i \frac{\alpha_m}{\alpha_m + < \alpha_i >} \tag{3.3}$$

in which α_m and α_i are the mirror and material losses, respectively and η_i is the injection efficiency, namely, the fraction of injected carriers which enter in the active region.
In the frame of this empirical model, it is possible to climb back to the generation rate that, combined with the recombination rate, can effectively be used in order to understand the temporal dynamics of the carrier density inside the active region.
Obviously, this is only possible if one can rely on an accurate model of the dynamical behaviour of the QD structure knowing how does it behaves under a condition of carriers injection, how does it interacts with wells and wetting layers etc.

	A		B		C	
	I_{th} [mA]	P_{max} [mW]	I_{th} [mA]	P_{max} [mW]	I_{th} [mA]	P_{max} [mW]
$0.6\,mm$	135	102	105	283	165	160
$1.0\,mm$	105	151	105	286	165	260
$1.5\,mm$	125	142	135	312	215	216
$2.0\,mm$	145	110	155	213	245	177

Table 3.1: Output power at 950 mA and threshold current values.

3.2 Gain spectra

The study of the amplified spontaneous emission (ASE) spectra is a crucial starting point for a full characterization of any semiconductor laser, since it provides a huge insight on the very basic information about the internal physical behaviour. The way in which carrier distribution responds at external stimuli and the way in which generation-recombination processes take place inside the active region are information contained in the below-threshold regime. The post-process of the ASE spectra leads to information about internal gain and losses, the change in the refractive index, the dispersion and much more.
In the following three different techniques for the evaluation of the gain spectra are shown and their pros and cons discussed together with the achieved results.

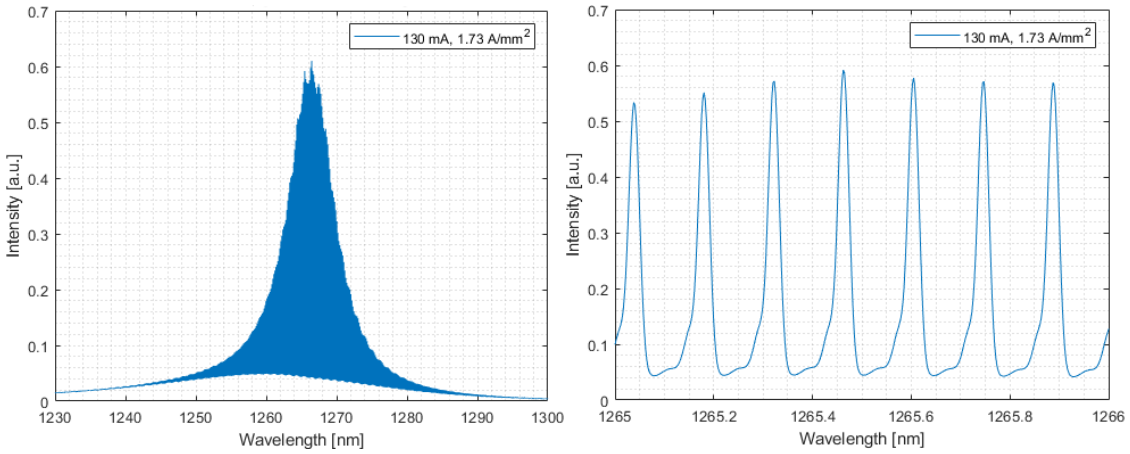

(a) Group B, 1.5 mm active region length.

(b) Zoom in.

Figure 3.4: Measured ASE spectra through FTIR method.

The behaviour of the *amplified spontaneous emission* shown in figure 3.4, under the approximation of uniform gain inside the cavity, can be written in the so called Fabry-Perot approximation [23][24]

$$I(\lambda) = \frac{B\left(1 + R \cdot e^{(\Gamma G - \alpha_{int})L}\right)(1 - R)}{\left(1 + R \cdot e^{(\Gamma G - \alpha_{int})L}\right) - 4R \cdot e^{(\Gamma G - \alpha_{int})L} \cdot sin^2\left(\frac{2\pi L n}{\lambda}\right)} \tag{3.4}$$

where B is the coefficient which count the total amount of spontaneous emission coupled inside the cavity, R is the reflectivity of the cavity facets, Γ confinement factor, G is the internal material gain, α_{int} are the internal material losses and L the active region length.
The techniques implemented for the gain extrapolation rely on equation 3.4 and in the following they will be discussed in details.

3.2.1 Hakki-Paoli method

In 1975, B. Hakki and T. Paoli [22] proposed a method to determine the modal optical gain of a semiconductor junction by means of the depth of the modulation in the amplified spontaneous emission spectra of the Fabry-Perot resonances.

$$g(\lambda) = \Gamma G = \frac{1}{L} \ln \frac{\sqrt{r(\lambda)} - 1}{\sqrt{r(\lambda)} + 1} - \frac{1}{L} \ln R \tag{3.5}$$

where $r(\lambda)$ is introduced as peak-to-valley ratio

$$r(\lambda) = \frac{I_{max}(\lambda)}{I_{min}(\lambda)} \tag{3.6}$$

with I_{max} and I_{min} maximum and minimum value of equation 3.4.

In fact, is easy to notice how simple and fast this method is, the main limitation is that the cavity is required to have a moderately high Q-factor. As the resonance starts to be more fitted in wavelength, experimental limitations arise, for the correct evaluation of the gain spectra, the fringe contrast has to be well defined.
Nevertheless, for interferometer which allow the detection of *free spectral range* (peak-to-peak wavelength distance) as low as 0.1 nm, the introduced error is negligible.

Another factor that must be taken into account with the Hakki-Paoli method is the high instrument sensitivity. The selection of a single wavelength by means of a monochromator carries a response function that has to be considered in the post-process. The main issue is to select a proper response function to be convoluted with the measured data, it is strongly dependent on the measurement setup and the machine itself.
In our case the measurements were unaffected by this kind of behaviour, in fact any correction which was applied during the post-processing seemed to be ineffective on the results.
This could be attributed to the fact that the ASE spectra were acquired not by means of an output monochromator, but by means of an interferometric setup as explained in Chapter 2.

The overall post-process were carried by scripting the code by only giving as input the ASE spectra for each investigated injection current

3.2.2 Mode Sum method

In 1984, a paper proposed by D. Cassidy [23] discussed a slight different method for the evaluation of the gain spectra, which is demonstrated to be less sensitive to the measurement setup than the Hakki-Paoli method.
It still relies on the ASE spectra and the Fabri-Perot resonances

$$g(\lambda) = \Gamma G = \frac{1}{L} \ln \frac{p(\lambda) - 1}{p(\lambda) + 1} - \frac{1}{L} \ln R \tag{3.7}$$

where in this case $p(\lambda)$ is the ratio between the integral over one mode and the mode minima.

$$p(\lambda) = \frac{1}{I_{min}(\lambda)} \cdot \frac{\int_{\lambda_1}^{\lambda_2} I(\lambda')\, \mathrm{d}\lambda'}{(\lambda_2 - \lambda_1)} \tag{3.8}$$

As it can be noticed, the physical meaning of 3.8 is exactly the same as 3.6. In this case the integration over every FSR allows to overcome the peak detection problem which arise when dealing with high quality factor devices.
Here as well, a convolution technique is adopted to avoid error in the gain spectra evaluation.

A very clear and useful summary about pro and cons of these two techniques can be found in [24], where the measurements of semiconductor laser physical parameters are discussed. The final remark is that both Hakki-Paoli and Cassidy methods are pretty easy and fast to apply, the issues that we have discussed above are no longer of interest since the instrumentation used for the acquisition of ASE is way better then the one used in [22] and [24]. For what concern the spacing in wavelength, the spectrometer can be pushed far beyond the FSR, thus no minimum/maximum detection problem has to be solved.
In this characterization process, the VERTEX 80V from Bruker allowed to scan with a spectral resolution of 0.01 cm^{-1} which can be pushed at 0.0075 cm^{-1}. It must be noticed that a single scan with this power of resolution, depending on the wavelength range in analysis, could also take hours. Since measurements were repeated for every sample, for several injection current and temperature conditions, a balanced compromise was reached: a discrete number of equispaced injection current were measured, with a particular attention on the very edge of threshold for purpose that we will discuss later on.

3.2.3 Fourier Transform Analysis method

The last technique we are approaching to explain were proposed in 1999 by Hofstetter [25], a method which does not have any constrain on Fabry-Perot interference fringes, and therefore, more versatile. Moreover, from this method it is straightforward to retrieve delay dispersion and refractive index parameters.

By imposing $\beta = 1/\lambda$, we move in the wavenumber domain

$$I(\beta) = \left(\frac{1-R}{\sqrt{R}}\right)^2 \frac{2b}{1-b^2} \cdot \sum_{m=0}^{\infty} b^m \cdot cos(4\pi nL\beta m) \tag{3.9}$$

Equation 3.9 is a rearrangement of the Airy formula, that is the representation of 3.4 in the wavenumber domain. The physical meaning of the above equation can be found if we think of it as an infinite sum of shifted Lorentzian peaks, which is then represented as cosine functions series.

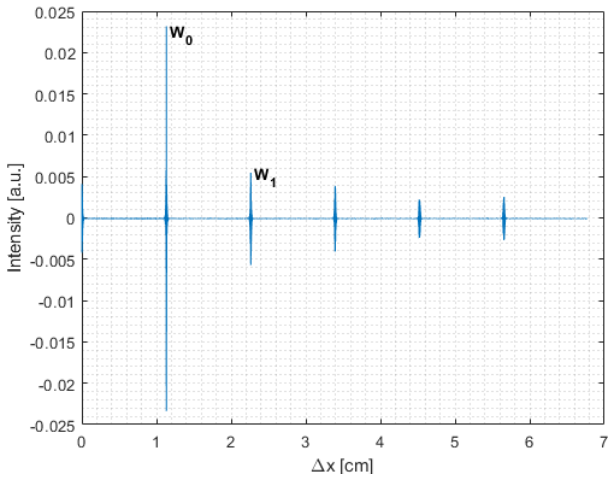

Figure 3.5: Measured interferogram spectra through FTIR method.

Therefore, by applying a Fourier transform

$$I(d) = \int_{-\infty}^{\infty} I(\beta) e^{-i2\pi\beta d} \mathrm{d}\beta \tag{3.10}$$

we obtain the following result

$$I(d) = \left(\frac{1-R}{\sqrt{R}}\right)^2 \frac{1}{4nL} \cdot \sum_{-\infty}^{\infty} W(d)_m \cdot \delta\left(\frac{d}{2nL} - m\right). \tag{3.11}$$

Equation 3.11 should ideally be a series of exponentially decaying delta-peaks with harmonic amplitude ratio b. If we let b being dependent on wavelength, the peaks are no more δ-shaped, in this frame b is stated to be

$$b(\beta) = R \cdot e^{-[\alpha - g(\beta)]L} \tag{3.12}$$

The mathematical derivation that leads to equations 3.11 and 3.12 is way more complex and far from the thesis purpose.
Nevertheless, the effect of the wavelength dependence of b has a simple physical meaning: the δ-peaks spread in peaks which shape is given by the Fourier transform of the pre-factor $2b/(1-b^2)$ in equation 3.9. This shape factor is the $W_m(d)$ term in equation 3.11, and the inverse transformation of the ratio between two adjacent harmonics, $m+1$ and m, gives as result

$$b(\beta) = \frac{\int_{-\infty}^{\infty} W(d)_{m+1} \cdot e^{i2\pi\beta d} \mathrm{d}d}{\int_{-\infty}^{\infty} W(d)_{m} \cdot e^{i2\pi\beta d} \mathrm{d}d} \tag{3.13}$$

In figure 3.5 it is easy to see the no more δ-peaks spread, the interferogram was obtained by FTIR technique as already discussed. From the practical point of view, the algorithm for the evaluation of the gain spectra relies on equations 3.11 and 3.12.
The Fourier anti-transform are operated on the second and first peaks, respectively W_1 and W_0. Then, their ratio returns the gain spectra with a way higher insensitivity to the instrumentation with respect to the first two methods presented so far.
Is also important to notice that, the shape function of the first harmonic term (described by the shape function W_1), retains important information which will be discussed later.

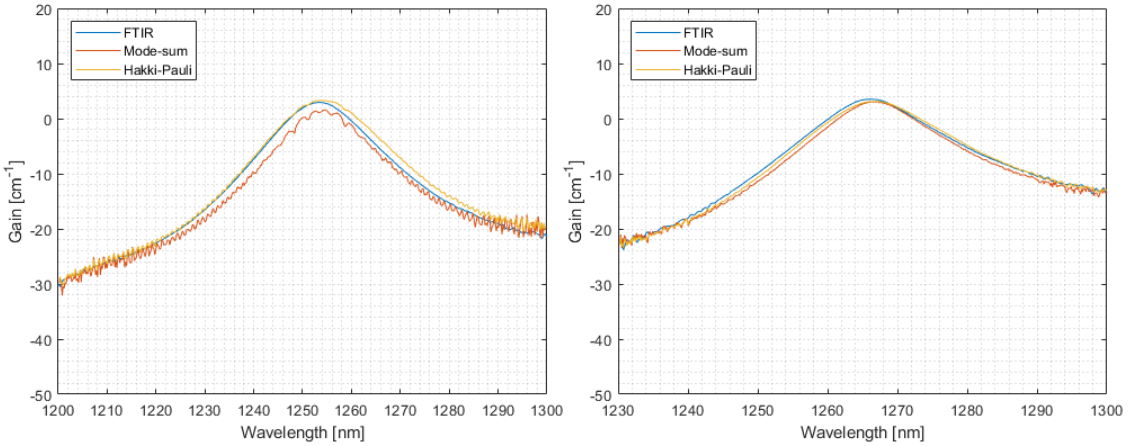

(a) Group A, 1 mm active region, 95 mA.

(b) Group B, 1.5 mm active region, 130 mA

Figure 3.6: Methods comparison.

Figure 3.6 shows the results of the three techniques discussed so far applied on undoped and mild-doped devices, with 1 mm and 1.5 mm active region length respectively.
The results are almost overlapped, the maximum shift for the gain is $\Delta g = 2$ cm^{-1} and the central wavelength shift is, in the worst case, in the order of the nanometer. Around 1250 nm, the interferometer precision is evaluated to be ~ 0.02 nm, thus, an order of magnitude lower than the measured 0.1 nm FSR for the 2.0 mm active region length device. If one takes into account that the FSR of a Fbry-Perot interferogram decreases for longer active region lengths, it is reasonable to expect that, for shorter devices, the two techniques ten to give lower mismatches.

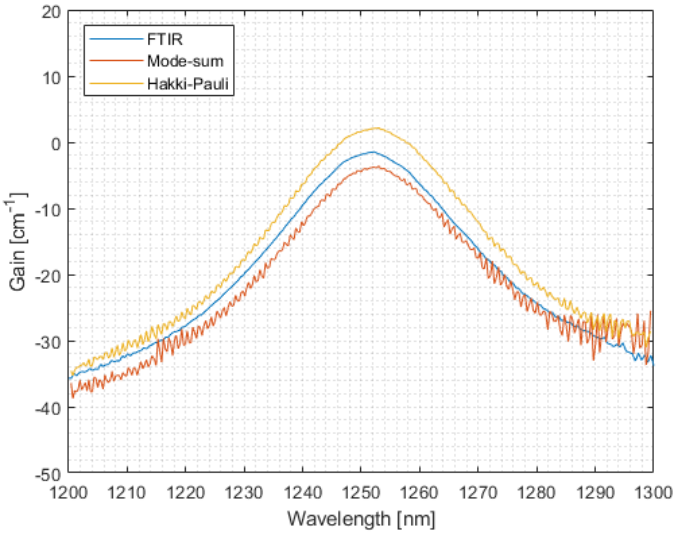

Figure 3.7: Methods comparison for the 0.6 mm, group A, @100 mA.

In figure 3.7, the methods comparison for a 0.6 mm active region length, undoped devices, is depicted. The results show a much higher mismatch for both gain maxima and central wavelength, on the contrary of what is stated above. In this case, the FSR is measured to be ~ 0.3 mm, therefore far above the spectral resolution.
Thus, as stated in section 3.2.2, being the resolution of the Fabry-Perot peaks distance excluded as a limitation for these techniques, the explanation for the over- and under-estimation of Cassidy and Hakki-Paoli may be found on the fact that, for shorter devices the collimation of the beam inside the interferometer become more difficult as a consequences of the wide beam profile, which will be discussed in section 3.5. This technological issue forces the instrumentation to work with low input power, bringing inaccuracy on the detection of the maxima and minima in the resonance peaks. This strongly affects the post-process for those methods which directly relies on the detection of the amplified emission spectra maxima and minima, such as 3.6 and 3.8.

Nevertheless, it is important to remark that Hakki-Paoli and Cassidy techniques are way faster and easier to implement and this is important especially when the sub-threshold characterization has to be performed on a very dense range of injection current. In the latter case the computational time required for the Fourier transform analysis could not be affordable. Once calculated the FSR, the power resolution of the instrumentations and, most importantly, once the power losses due to collimation process are the lower as possible, one can properly choose the best-fitted post-process technique.

3.2.4 Group Delay Dispersion

The group delay dispersion is a quantity used in order to give a measure of the chromatic dispersion of the medium in which the light is propagating. It is defined as the second derivative of the optical phase

$$GDD = \frac{d^2\phi}{d\omega^2} \tag{3.14}$$

As already mentioned, the shape function of the first harmonic peak allows to evaluate material parameters such as the refractive index, the phase of electromagnetic wave propagating and, therefore, the dispersion of the medium.
The inverse Fourier transform of $W1$ results in a complex function, which phase $\phi(\beta)$ yields

$$\phi(\beta) = 4\pi n(\beta) L\beta. \tag{3.15}$$

The retrieval of the refractive index, and group delay dispersion from the interferogram is therefore straightforward. Is important to put attention on the evaluation of equation 3.15: since the interferogram cannot be measured in the full range of β, an unknown offset in the phase value arises. This technological issue is overcome by a proper knowledge of the material refractive index.

	A	B	C
	GDD [fs^2]	GDD [fs^2]	GDD [fs^2]
0.6 mm	-2000	-2000	-2000
1.0 mm	-4000	-3000	-3000
1.5 mm	-6000	-5000	-5000
2.0 mm	-7000	-7000	-7000

Table 3.2: Group delay dispersion peak values.

The full set of results about GDD can be found in Appendix A.6.
Table 3.2 shows the values collected at the central wavelength emission. It is easy to notice how the GDD is almost insensitive to the doping condition of the devices, while the active region length affects it.

3.3 Results discussion and consideration

In the previous sections, the techniques used for the post-processing of the raw-data were described in order to clarify pros and cons of each one. Hereafter, the results of the whole set of lasers will be discussed in details.
The behaviour of the maxima modal gain for each devices is depicted in appendix A.4 and A.5. The values were taken in the very proximity of the stimulated emission region of operation, therefore, the values on the above graphs can be also taken as a reference for the current density threshold values.
The x and y axis are chosen to be of the same scale, to the detriment of the clarity, in order to better understand the effects of the doping and different active region lengths.

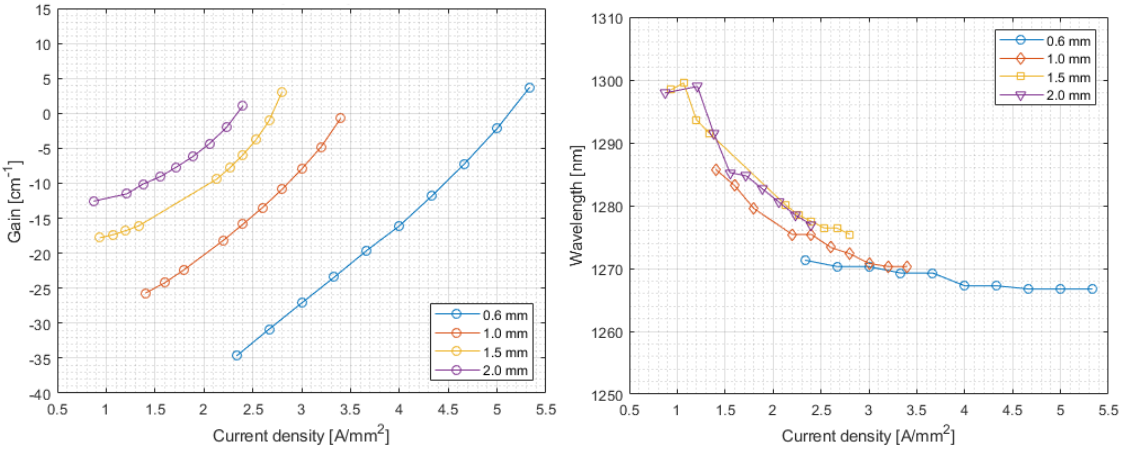

(a) Maximum gain.

(b) Central wavelength shift.

Figure 3.8: Data selection from group C lasers.

In section 2.1 we discussed about threshold values and optical output power. In that frame, the length of the active region acts in such a way that the shorter devices (0.6 mm) always behave worst than the longer devices: lower output power, lower wall plug efficiency and higher threshold current.
Nevertheless, talking about the gain spectra, the shortest devices exhibit almost optimal behaviour: the carrier confinement in QD is expected to bring more symmetric and peaked gain curves, as will be explained later. From the measurements, the 0.6 mm long active region length in QD devices brings the gain to behave more-likely to what predicted by the theory.
As an example, figure 3.8 reports the summary of the trend for net modal gain maxima and related wavelength, for the group C, in which is clearly visible that, reducing the active region length the central wavelength shift is reduced and the maxima gain undergoes a stronger increase. The central wavelength is referred to

the wavelength at which the maximum power emission is detected in the ASE, the insensitivity of this value from the current injection gives a good figure of merit to understand a-priori the shape of the gain curves.
A more detailed exposition of the whole post-process data, as well as the behaviour of the full set of gain spectra, can be found in appendix A.3.

3.3.1 α parameter considerations

Is noticeable that, for what concern the 0.6 mm active region length, while the red-shift of the lasing wavelength is $\sim$ 6 mm, the values range in which the gain maxima spaces is very wide (~ 40 cm^{-1}).
This kind of behaviour is important because it indicates the linewidth enhancement factor. Such a parameter, also known as α parameter, directly related the variation of the refractive index with the carrier concentration inside the active region, also is crucial for the dynamic behaviour of the device and so on and so forth.
From a computational point of view, we can evaluate the linewidth enhancement factor as

$$\alpha = -\frac{4\pi}{\lambda}\frac{\delta\tilde{n}/\delta I}{\delta g/\delta I} \tag{3.16}$$

where $\tilde{n}$ is the modal index, which can be evaluated from the shift of each Fabri-Perot modes in the ASE, as function of the injected current.
Unfortunately, for what concern the very peaked gain spectra from the 0.6 mm devices, the shift of the wavelength is way lower than the resolution in wavelength of the measured ASE. Therefore, a Lorentzian model is proposed as a solution. A more complete and detailed treatment of this topic can be found in [29], where the modal index variation is evaluated by fitting the ASE spectra and by also taking in consideration the temperature induced variation with a simple model.
The full characterization of the linewidth enhancement factor would require several more dedicated measurements of the below-threshold behaviour, as well as a dedicated post process analysis which, due to the amount of devices in study, are not performed yet.
In here we can just observe that, for lower index variation and for high increase of the net modal gain maxima, equation 3.16 tends to zero. The zero value of the α factor is predicted for QD laser, on the assumption of symmetric gain spectra with a reduced wavelength chirp. The physical reason is to be searched in the electronic structure of the dots and the strong confinement they brought to the carriers [28].
The behaviour for the gain spectra described above, can be recognized in the devices with 0.6 mm long active region length, independently of the doping concentration, which gives a good starting point for a deeper investigation of the α factor for the whole set of lasers.

3.3.2 Gain shift phenomena

Another observation made on the complete set of results is the unusual behaviour of the gain spectra, which undergoes a down-shift for shorter devices. Being the comparison performed on the very same devices with identical injection current *density*, the expected result should be a full overlapped gain spectra, but the comparisons show a different trend.

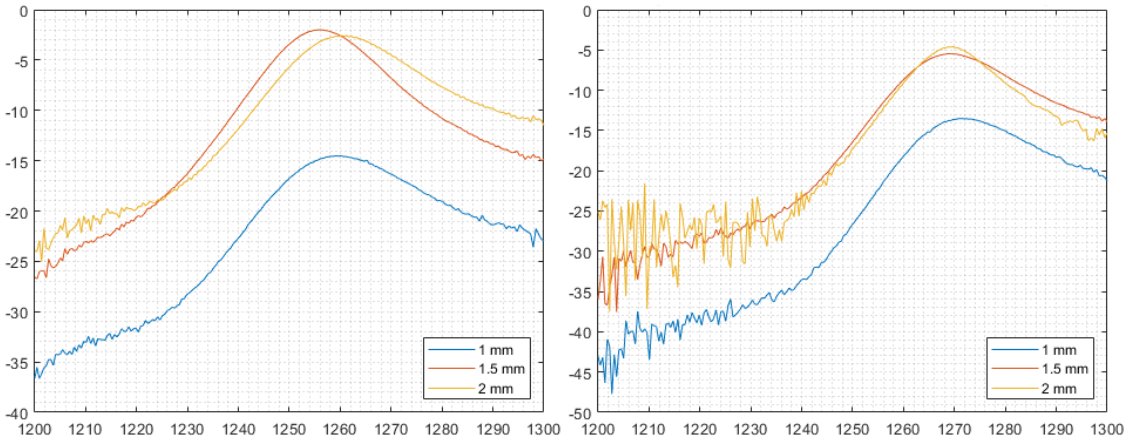

(a) Group A, 1.20 A/mm^2.

(b) Group B, 1.50 A/mm^2.

Figure 3.9: Gain evaluated for the same devices, at the same level of injection.

In figure 3.9 is reported the behaviour of the undoped and mild doped devices, for each active region length a current for which the total carrier injection results the same is chosen. Is noticeable as the shape of the spectra profile is almost the same for every devices, small difference can be attributed to measurements fluctuation or post-processing limitation, but the most relevant difference is in the strong shift of the whole spectra, which is measured to be in the order of $\sim 10\,cm^{-1}$. In the case of same substrate and same QD growth process, being the gain a quantity which should be independent to the length of the active region, an explanation how this phenomena is required.
Once the trivial possible issue, such as wrong post-processing or issues related to the experimental setup, were discarded the approach chosen is to investigate an eventual broad area effect on the propagating modes inside the active region cavity, which will be discussed in section 3.5.

3.4 Temperature dependence

In order to make the whole characterization consistent as much as possible, some measurements were performed at different temperature condition.
The value of injection current for each measurement, is taken just below the lasing threshold, the temperature values chosen were $15°C$, $20°C$ and $25°C$. Being $25°$ the standard temperature of the characterization carried on so far, by choosing two more operation temperature one can be able to observe a trend of the most important figure of merits.
Taking in consideration the experimental measurements time and the time needed to the set-up to reach and maintain the temperature condition with a proper degree of reliability, the number of devices investigated is limited with respect the whole set.
In figure A.15 the gain spectra at near threshold are reported as function of temperature.

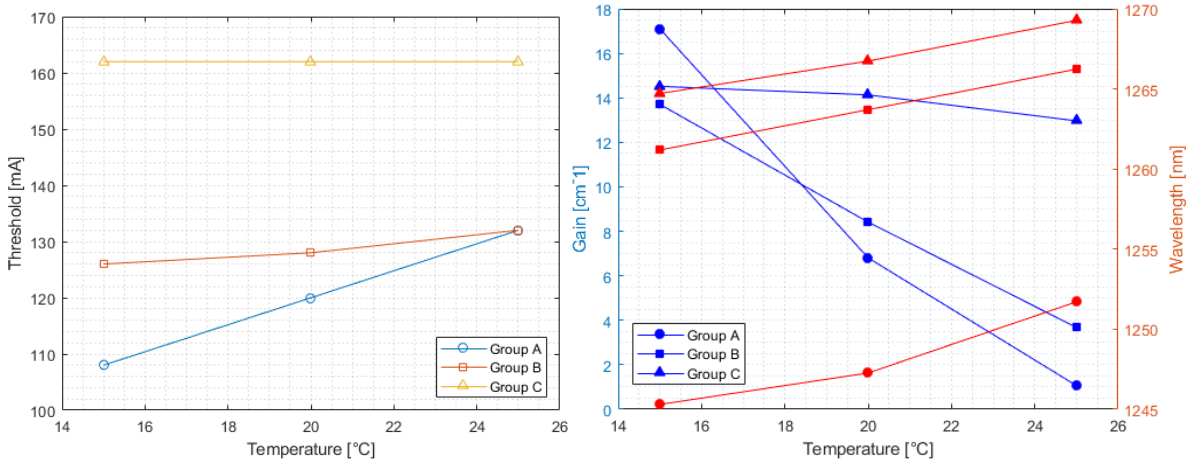

(a) Threshold current.

(b) Max gain and central wavelength.

Figure 3.10: Physical parameters trends as function of temperature.

In figure 3.10 a summary on the behaviour of our lasers is shown. As predicted in literature, the doping level has a strong impact on temperature sensitivity of lasers' figure of merits.
Analysing figure 3.10 (b), it is easy to see how the central wavelength is affected almost in the same way, no matter the doping concentration. For higher temperature, there is a noticeable red-shift for the emission wavelength with an increase of $\sim 2.5\,nm$ for the doped devices and $\sim 5\,nm$ for the undoped one. The behaviour is mirrored for lower temperature, where the blue-shift results in a decrease of $\sim 2.5\,nm$ for doped devices and $\sim 5\,nm$ for the undoped laser.
For what concern the maximum gain values evaluated just below threshold, is

noticeable how the doping modulate the temperature dependence. For undoped device, is measured a gain decrease of $18\,cm^{-1}$, while for the higher doping concentration the reduction fall to $\sim 1\,cm^{-1}$.
This huge difference justifies further analysis on the benefit introduces by the doping of wetting layer.

In figure 3.10 (a) the threshold currents for three devices with different doping concentration are compared. Also in this case, the doping level introduces benefits, the undoped device's threshold undergoes a strong shift due to temperature change. The trend for the threshold seems to be almost linear in all of the three cases, as the doping concentration increases the slope of the linear function sharply decreases. From the undoped to the middle doping devices the difference is huge, the sensitivity to the temperature is severely reduced. For the higher doping level, no changes are reported for the threshold current.

From a theoretical point of view, the threshold temperature dependence is mainly due to parasitic recombination of carriers which do not contribute to lasing. In bulk and quantum well laser this phenomenon happens since the recombination take place between population which obey a Fermi-Dirac distribution, which gives a threshold temperature dependent.
Ideally, in QD active media the carrier recombination takes place between discrete levels in which there is no parasitic recombination. The modern heterostructure design involve the presence of the so called wetting layers, which provide the carrier injection inside the dots. This leads to a non-confined population which carries a current temperature dependence, this is the reason why, in figure A.15 there is a visible shift. Moreover, the statistical behaviour of shape and size in QD, complicates even more the picture of the electronic structure discussed so far.
Nevertheless, QD laser have shown a way better behaviour in temperature sensitivities with respect to QW and further improvements are found by inserting a dopant inside the wetting layer. A possible physical explanation on how the p-doping is so effective on sensitivity may be found on its direct effect on the spacing of the discrete energy level for holes inside the dots. A more detailed treatment of this topic can be found in [26], where undoped and p-doped devices are deeply analysed.

Some measurements were also performed to understand if the issue related to the gain spectra shift discussed in section 3.3.2 can be temperature dependent. The results are coherent with the considerations made so far for the temperature dependence: laser with the same injection density current and same doping level undergoes a shift which is the same, independently of the active region length.

3.5 Broad area effect

In the previous section, the basic sub-threshold figure of merits are investigated and the obtained results are reported and commented.
Hereafter the focus will be posed on the effect brought by the large width of the active region. By design, every device in the set has a $50\,\mu m$ width and, as a result, a multi-modal emission behaviour is reported.
Due to the broad area of the active region, several high order modes are guided, in these cases an issues that could arise is the collimation of the beam-profile within the instrumentation used for measuring, problem which is strictly related to the spatial coherence of the emitted field.
The investigation are performed in parallel with another identical devices, same structure and material, same doping concentration, but with an active region width of $5\,\mu m$.

3.5.1 Near-field beam profile

In order to verify the actual multi-modal nature, a near field measurements is carried out. A first measurement was performed by means of a setup in which the laser is brought above threshold and focused inside a NIR CCD camera, this procedure gives as a result the image of the near-field emission beam profile.

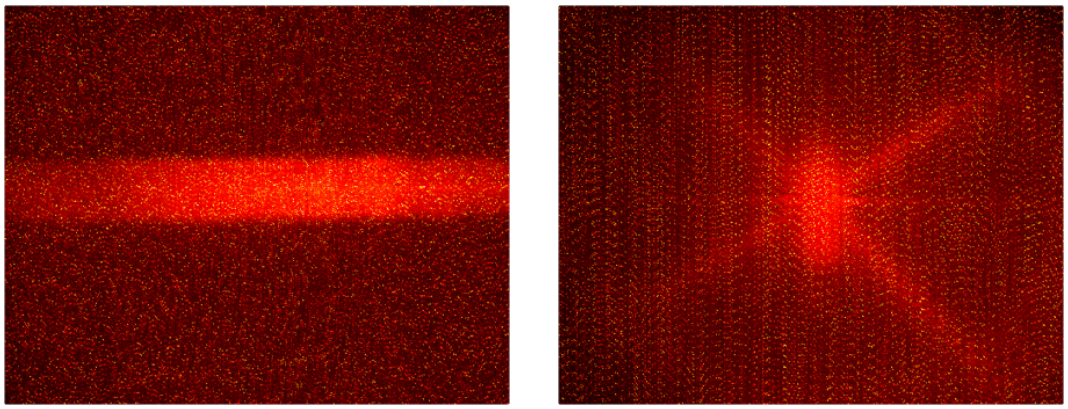

(a) Group C, $50\,\mu m$ broad area. (b) Group C, $5\,\mu m$ narrow ridge.

Figure 3.11: CDD camera maps for the near beam shape.

In figure 3.11 the measurements from the CCD camera are reported. The same setup is used for both the devices, the distance between the facet and the CCD camera objective kept fixed at $\sim 10\,cm$ and the measurements were performed at equal condition of temperature and room illumination. Therefore, within a certain error, it can be asserted that the plots 3.11 (a) and (b) are on scale.

The results clearly show how the beam shape of the wide ridge devices is spread along the longitudinal axis, while on the vertical one is narrow and similar to a single mode behaviour. On the other hand, narrow ridge device show a well defined single mode beam profile, which has a Gaussian-like shape in both cardinal directions.
In order to measure and verify the beam profile with a second technique, a single-mode fiber has been stepped through the laser beam using a step-by-step electro-mechanical engine. Thereby, for every step the light coupled into the fiber is measured by a power meter. By properly choosing the step and the acquisition time, the exact profile shape is measured

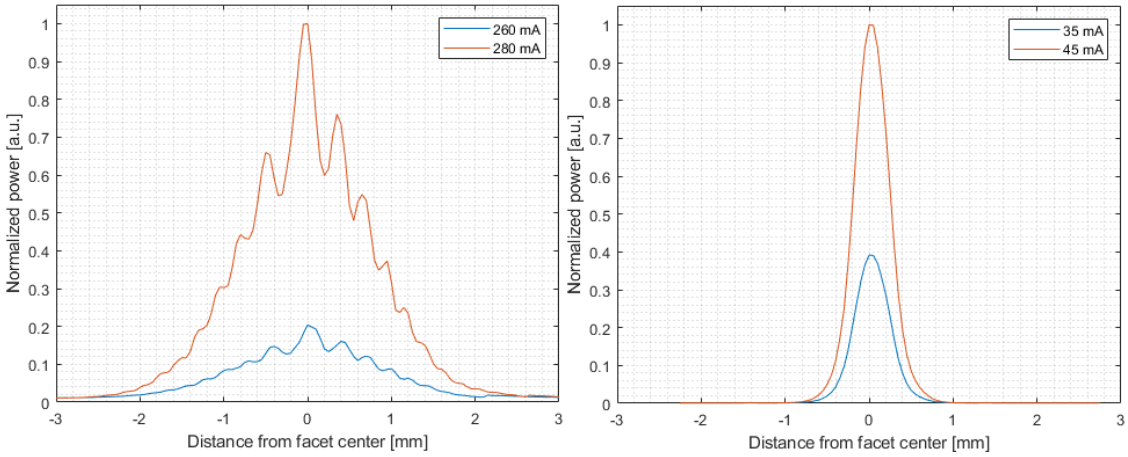

(a) Group C, 50 μm broad area.

(b) Group C, 5 μm narrow ridge.

Figure 3.12: Beam profile fiber scanned along the x-axis.

Figure 3.12 shows the results of the process described above. The scans were performed for both laser in both direction, in here is reported a couple of scan performed where the broad area effect takes place. As we can see, for the 50 μm width device depicted in 3.12 (a), high order lateral modes give rise to several power peaks in the emission field, while on the other axis the behaviour of the field is actually the same of the narrow ridge device, shown in 3.12 (b). This last case, is reported to have Gaussian-like beam profile in every scan directions and this yield a perfect single mode emission. Moreover, it is noticeable how, for increasing value of injection current, the high order mode arise and start to be more relevant in the profile shape.
Data shown in figure 3.11 and 3.12 are raw, no fitting and post process are involved. The characterization of the multimodal nature of our devices is a crucial step in the whole investigation, it allowed to take into account that, the measurements performed on the interferogram and on the amplified emission spectra below threshold, were not performed on the central mode, but also some of the higher order modes

were involved.
In order to quantify possible effect on the gain and related figures of merit, some measurements already performed and discussed in section 3.2 were ran again.

3.5.2 Far-field filtering

In order to screen the high order lateral modes, a filtering system was build up. The filtering of higher order modes below-threshold is not trivial at all: the set-up needs to be aligned and optimized for the maximum power detection, ensuring that only the central peak is measured. This can be a challenging task, when considering a beam profile as depicted in figure 3.12 (a).
In order to filter out everything but the central mode, two experimental solutions were approached. The first one involved the coupling of the output beam in a single-mode fiber which would act as a filter itself. A second approach involved a classical pin-hole far filtering setup. The scheme and concept of the latter, can be found in [31], where the same issues are investigated for an InGaAs-GaAs quantum well heterostructure.

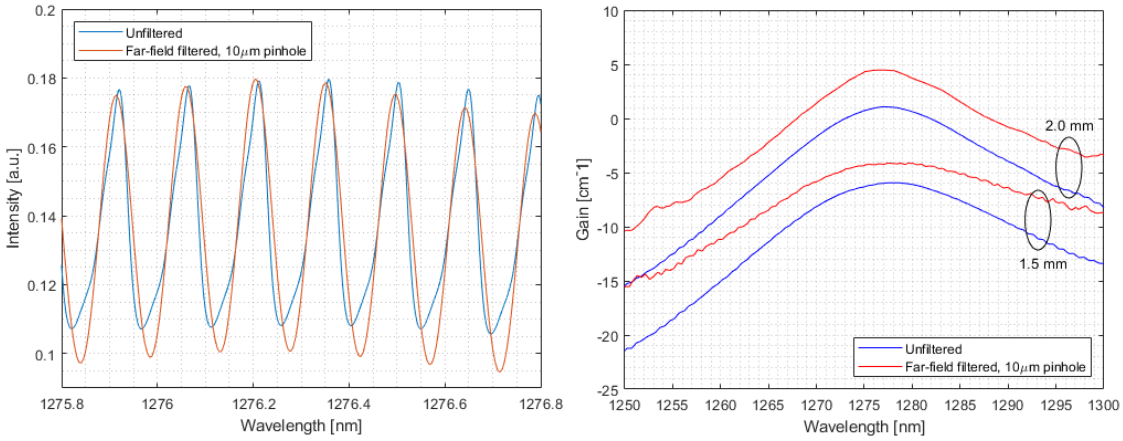

(a) Details of the ASE spectra.

(b) Effect on gain for two different devices.

Figure 3.13: Far-field filtering measurement results.

The comparison were made by running the acquisition of the ASE with and without filtering, for the same device on the same setup with the same working condition. Due to the amount of technological complication involved, the measurement is performed on the $1.5\,mm$ device from group C device at injection current density of $2.40\,A/mm^2$, just to be able to show the direct physical effect carried by the higher order modes. The spectra is chosen to be the one just below threshold, in order to maximize the power output and simplify the alignment procedure.
In figure 3.13 (a) exemplary zooms into the ASE spectra for filtered and unfiltered

measurements showing 7 modes are depicted, due to the filtering, the fringe profile of the ASE is modified, the minimum in the Fabry-Perot resonance peaks is reduced. Bearing in mind the discussion about the retrieval techniques in section 3.2, in particular equations 3.6 and 3.8, we recall the importance of the value of the valleys in the evaluation of the gain spectra. The high order modes cause a filling of the bottom ASE spectra, which brings an higher than expected I_{min} value, this results finally in a down-shifted gain spectra as depicted in figure 3.13 (b).
Also in this case, the measurement were performed on the very same devices, with the same carrier injection but different active region length, in order to verify if the mismatch between gain spectra, discussed in section 3.3.2, can be influenced by the broad area effect. In figure 3.13 (b) the comparison is shown: the shift seems to be rigid, the effect of higher order modes is stronger on the tails of the Lorentzian shape, filtering led a less broad peak but has no effect on the central wavelength of emission, which is unvaried. But the issue remains, the filling of the ASE bottom does not contribute to the gain spectra mismatch.

Appendix A

Backup images

A.1 PI curves

A.1.1 Active region length modulation

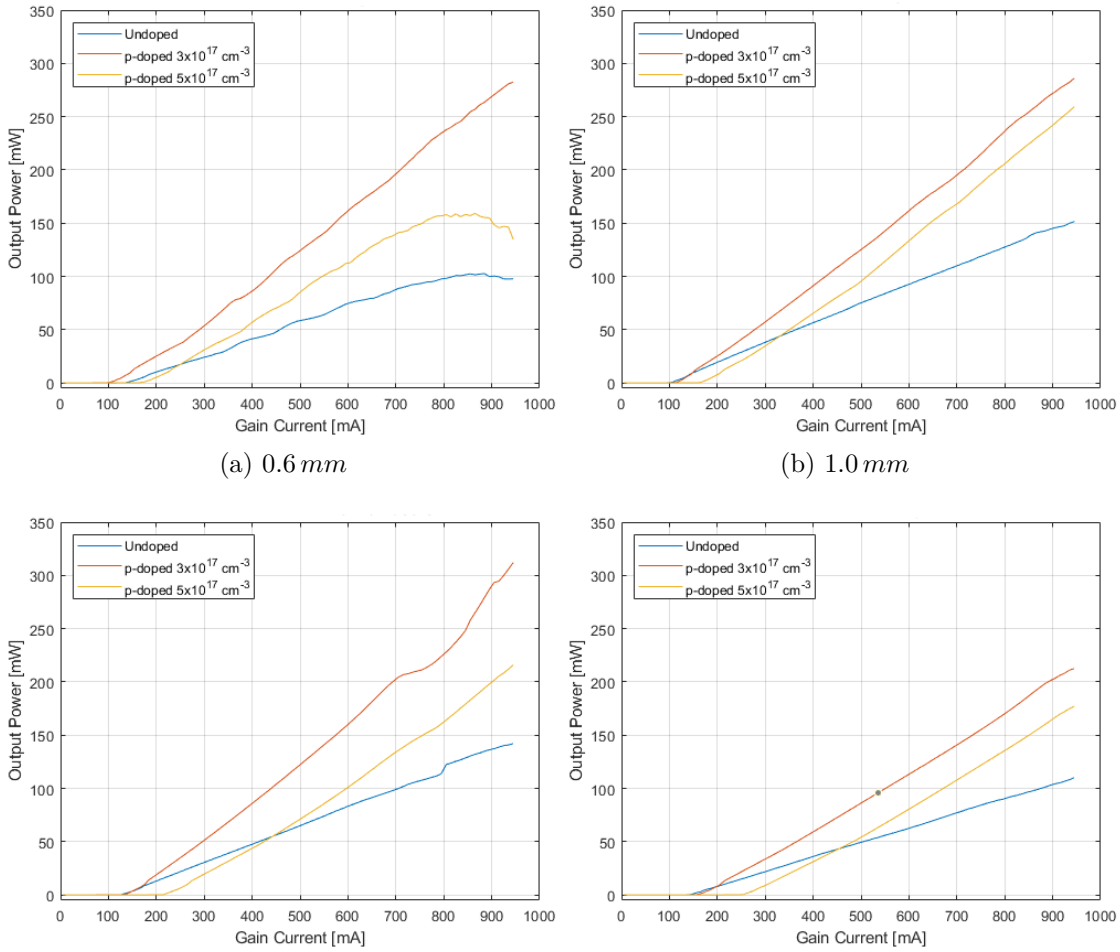

(a) 0.6 mm (b) 1.0 mm

(c) 1.5 mm (d) 2.0 mm

Figure A.1: P-I characteristics by active region lengths.

A.1.2 Doping level modulation

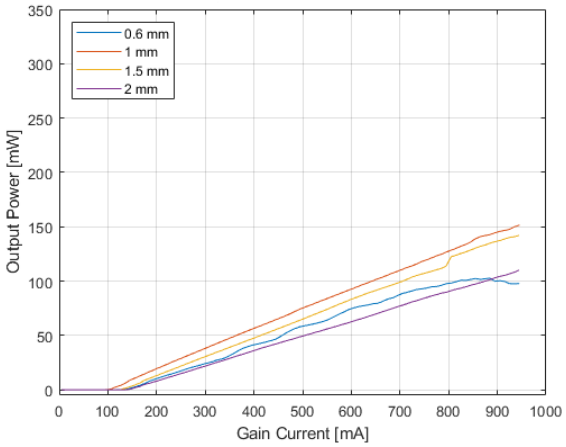

(a) Undoped

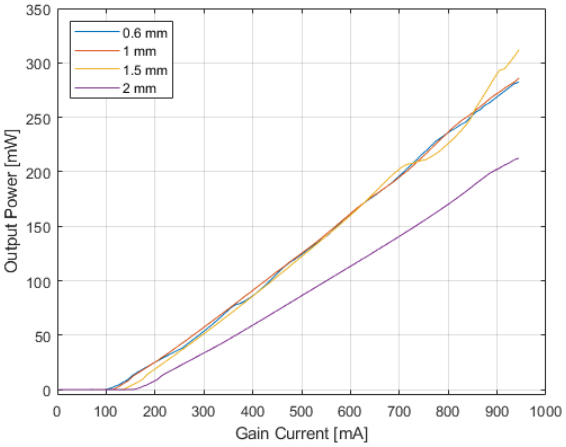

(b) $3 \times 10^{17}\ cm^{-3}$

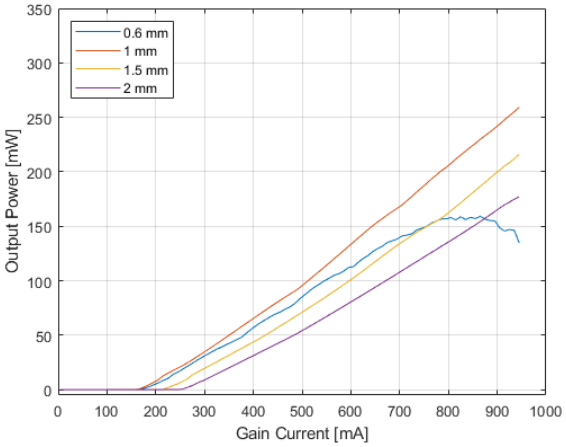

(c) $5 \times 10^{17}\ cm^{-3}$

Figure A.2: P-I characteristics by p-doping modulation.

A.2 Wall Plug Efficiency

A.2.1 Active region length modulation

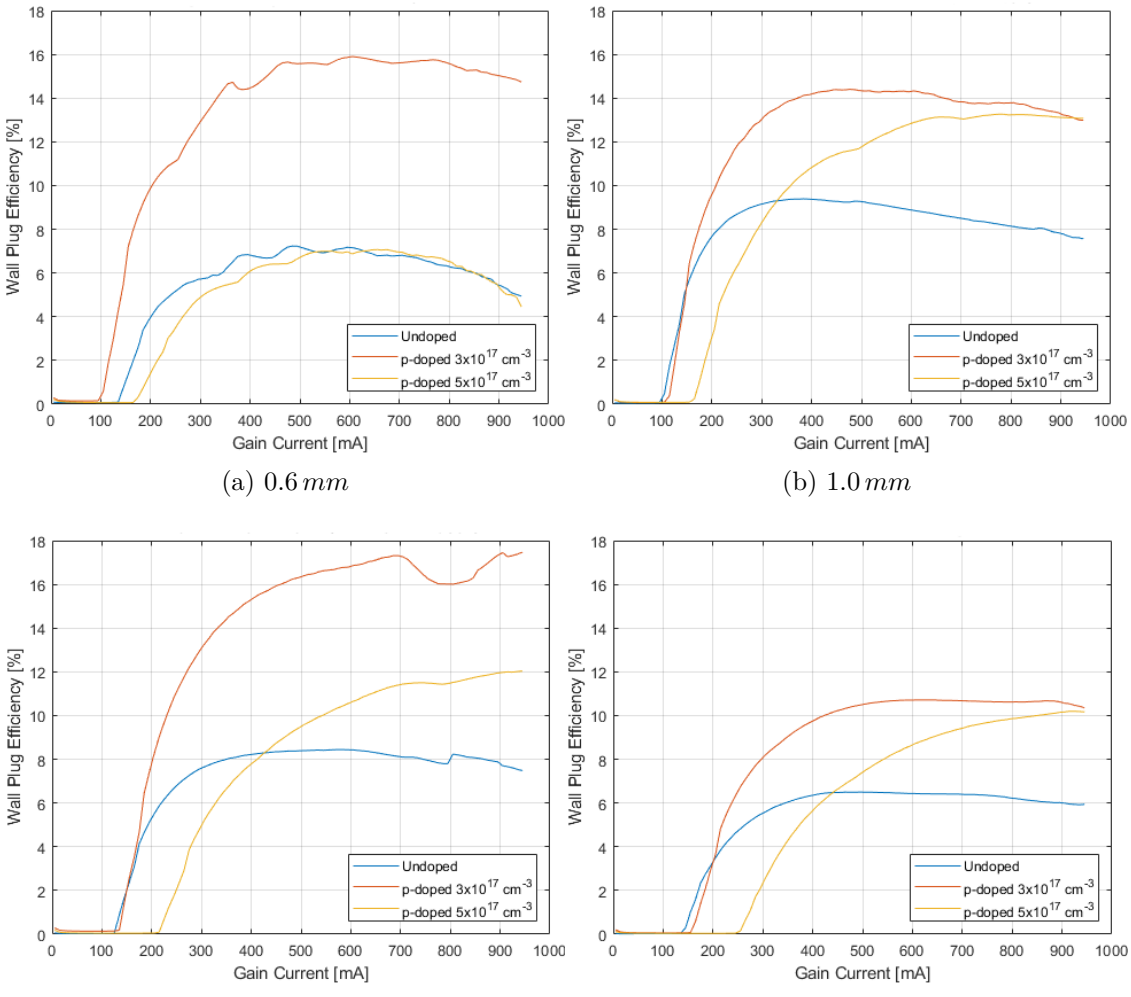

(a) 0.6 mm (b) 1.0 mm

(c) 1.5 mm (d) 2.0 mm

Figure A.3: Wall Plug Efficiency by active region lengths.

A.2.2 Doping level modulation

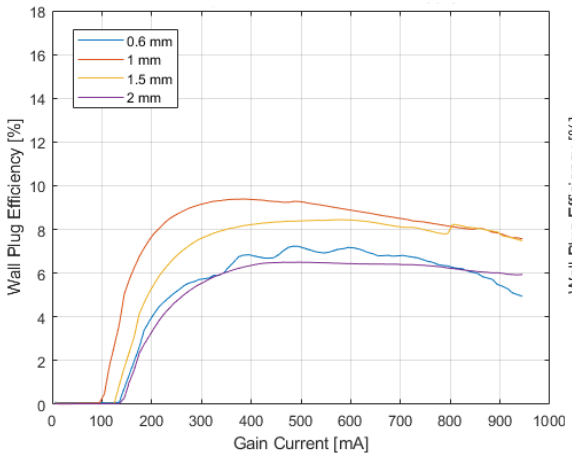

(a) Undoped

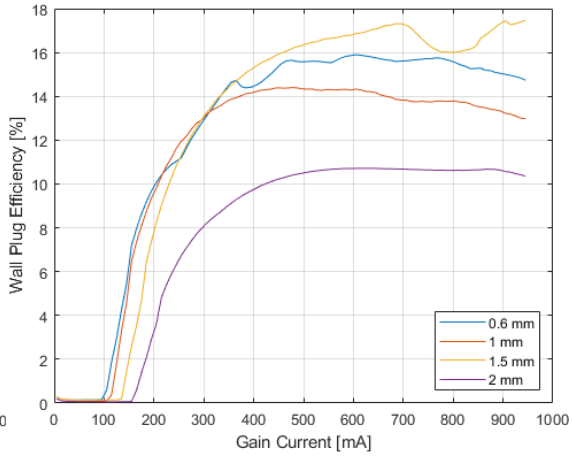

(b) $3 \times 10^{17}\ cm^{-3}$

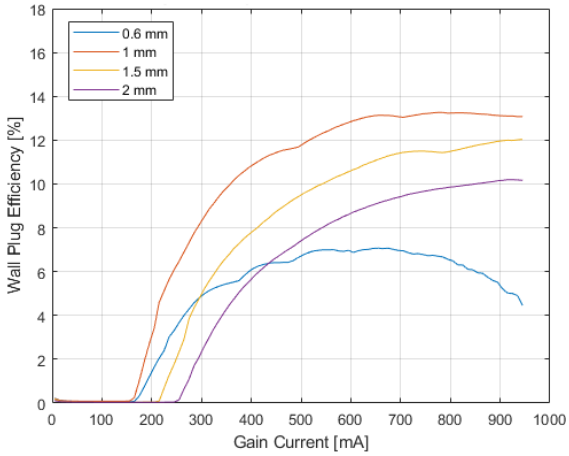

(c) $5 \times 10^{17}\ cm^{-3}$

Figure A.4: Wall Plug Efficiency by p-doping modulation.

A.3 Gain spectra

A.3.1 Group A

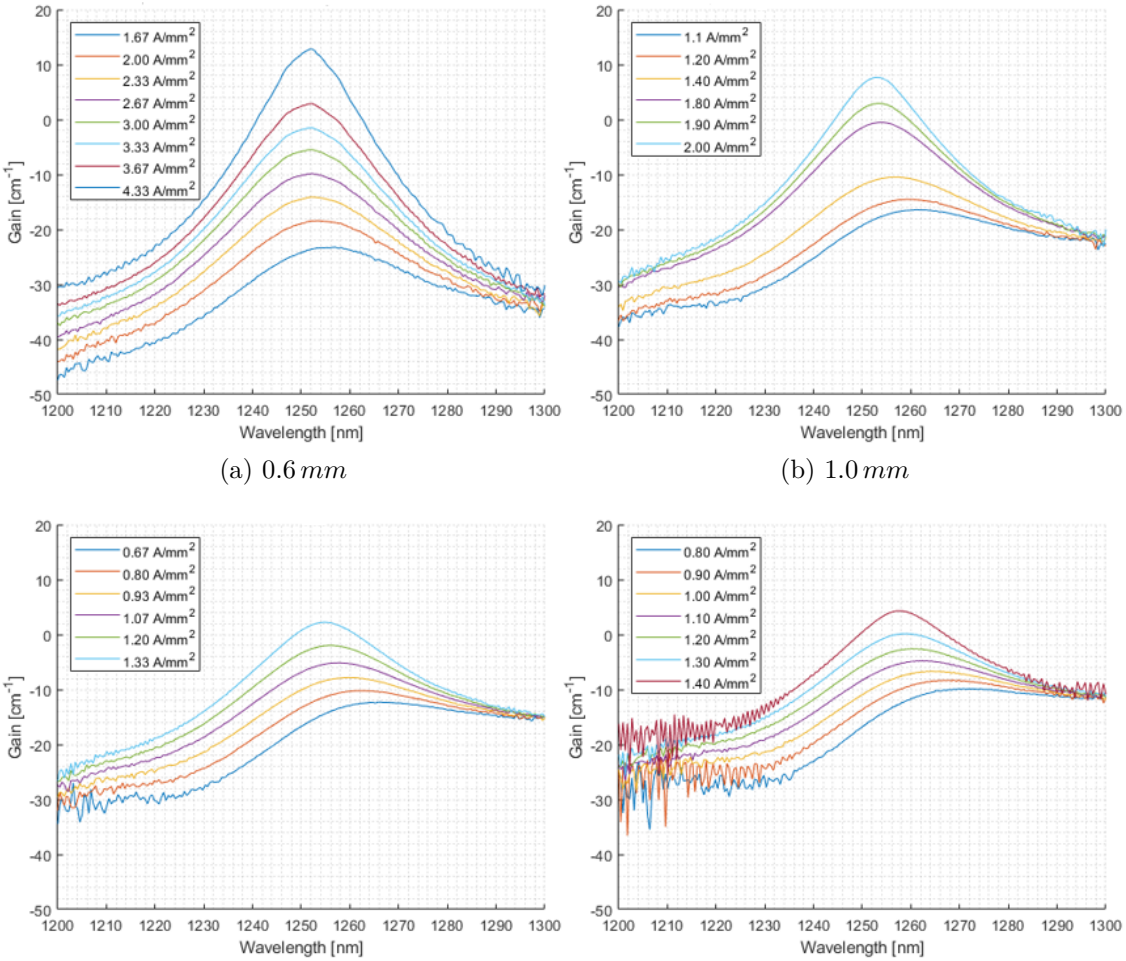

(a) 0.6 mm (b) 1.0 mm

(c) 1.5 mm (d) 2.0 mm

Figure A.5: Net modal gain spectra for the undoped devices.

A.3.2 Group B

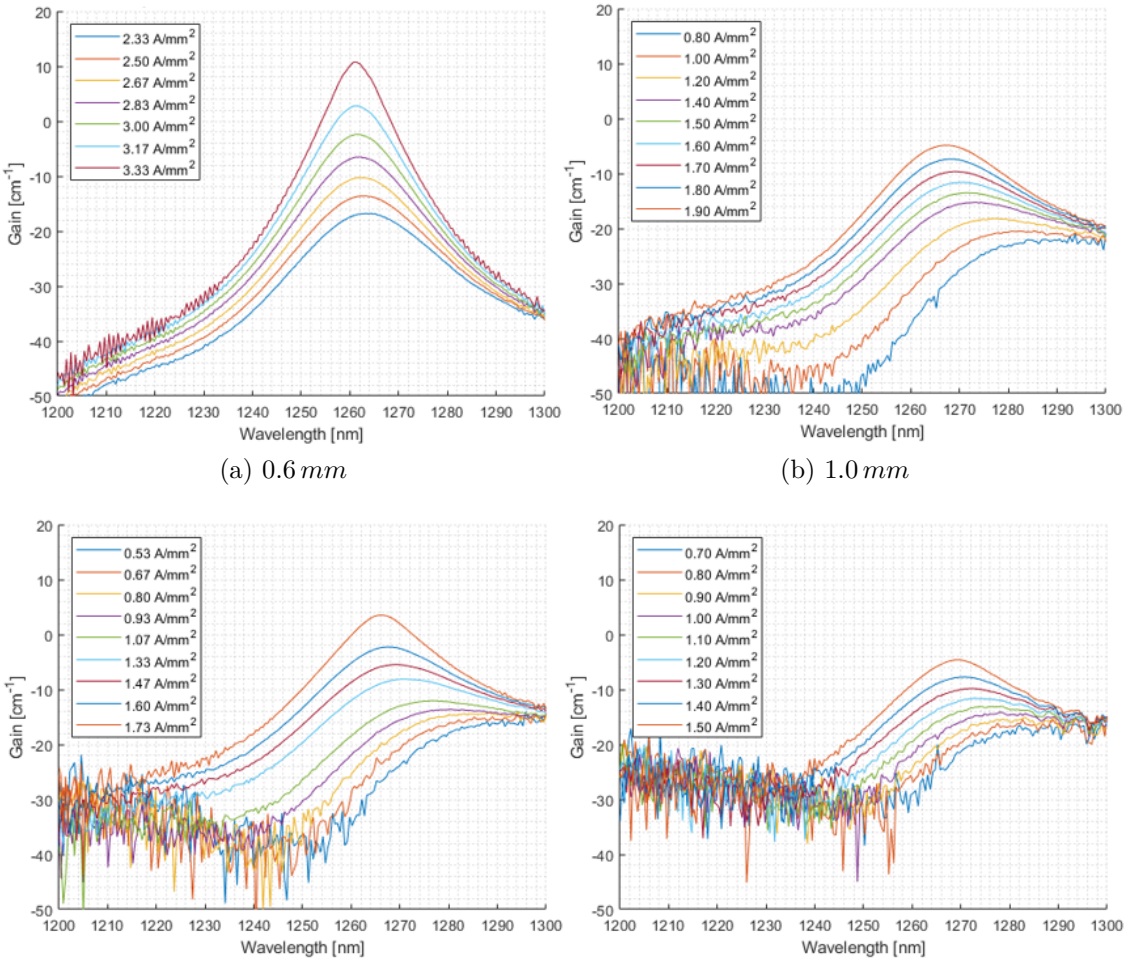

(a) 0.6 mm (b) 1.0 mm

(c) 1.5 mm (d) 2.0 mm

Figure A.6: Net modal gain spectra for the 3×10^{17} cm^{-3} doped devices.

A.3.3 Group C

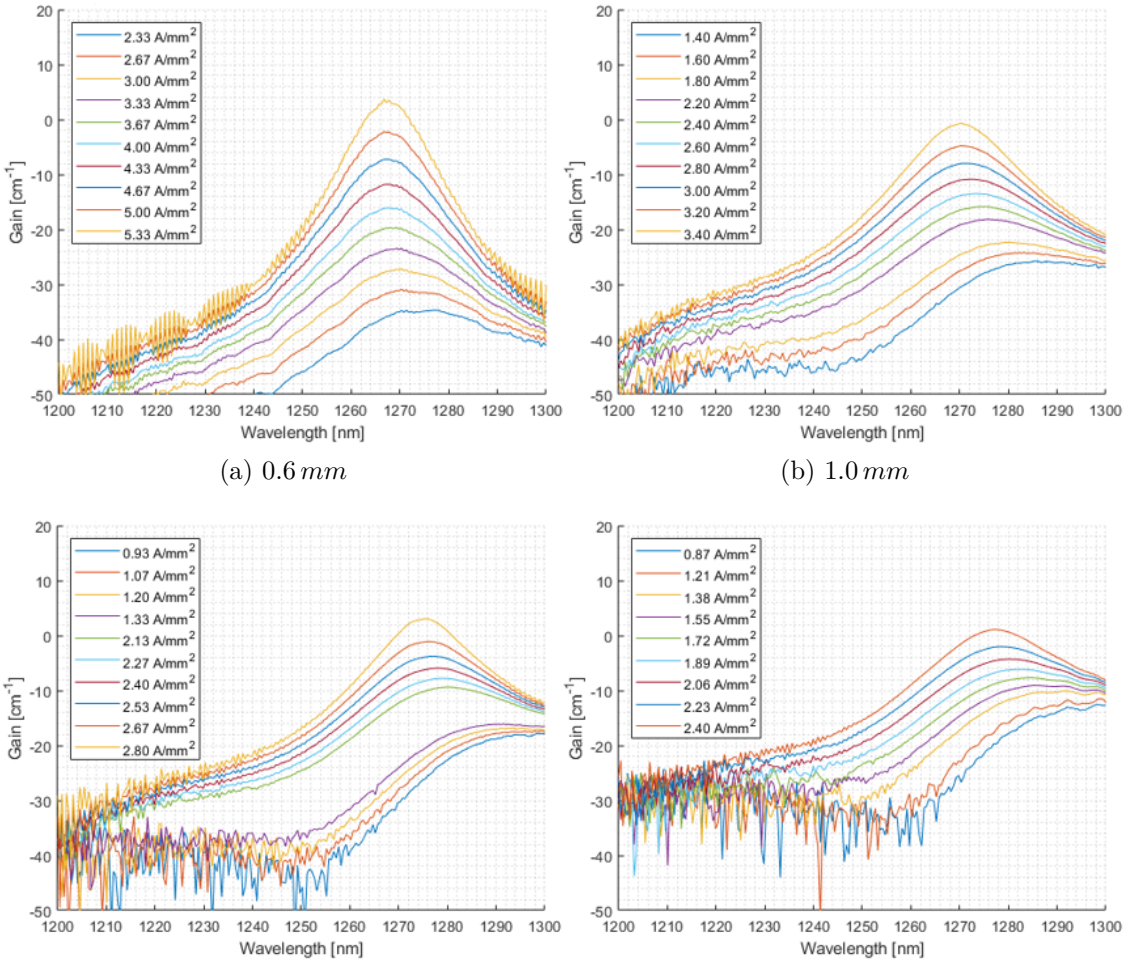

(a) 0.6 mm (b) 1.0 mm

(c) 1.5 mm (d) 2.0 mm

Figure A.7: Net modal gain spectra for the 5×10^{17} cm^{-3} doped devices.

A.4 Gain maxima

A.4.1 Active region length modulation

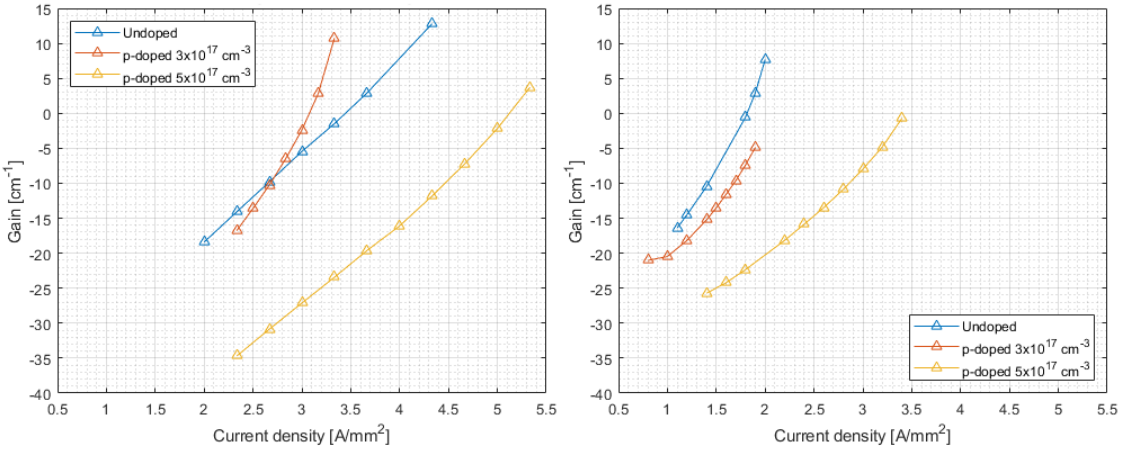

(a) 0.6 mm (b) 1.0 mm

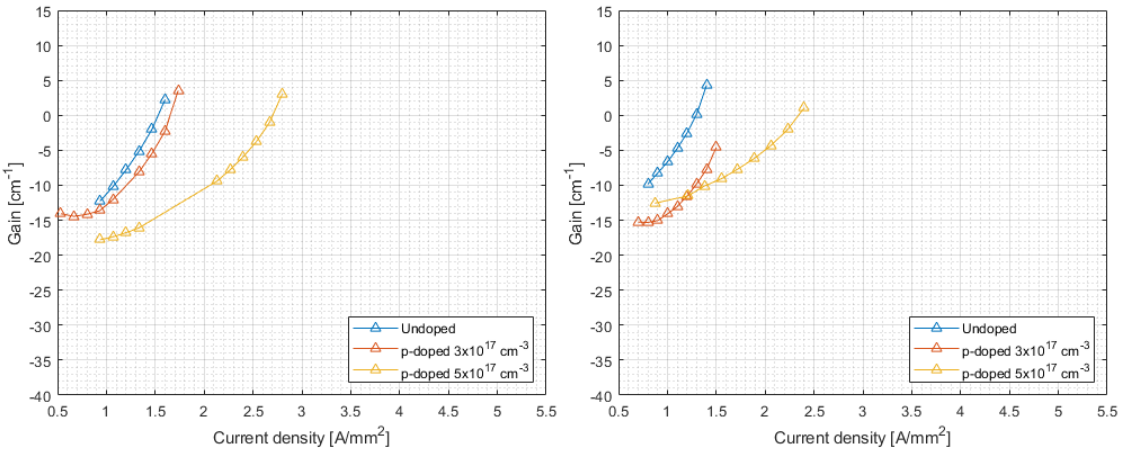

(c) 1.5 mm (d) 2.0 mm

Figure A.8: Maximum net modal gain as function of injection current, by active region length.

A.4.2 Doping level modulation

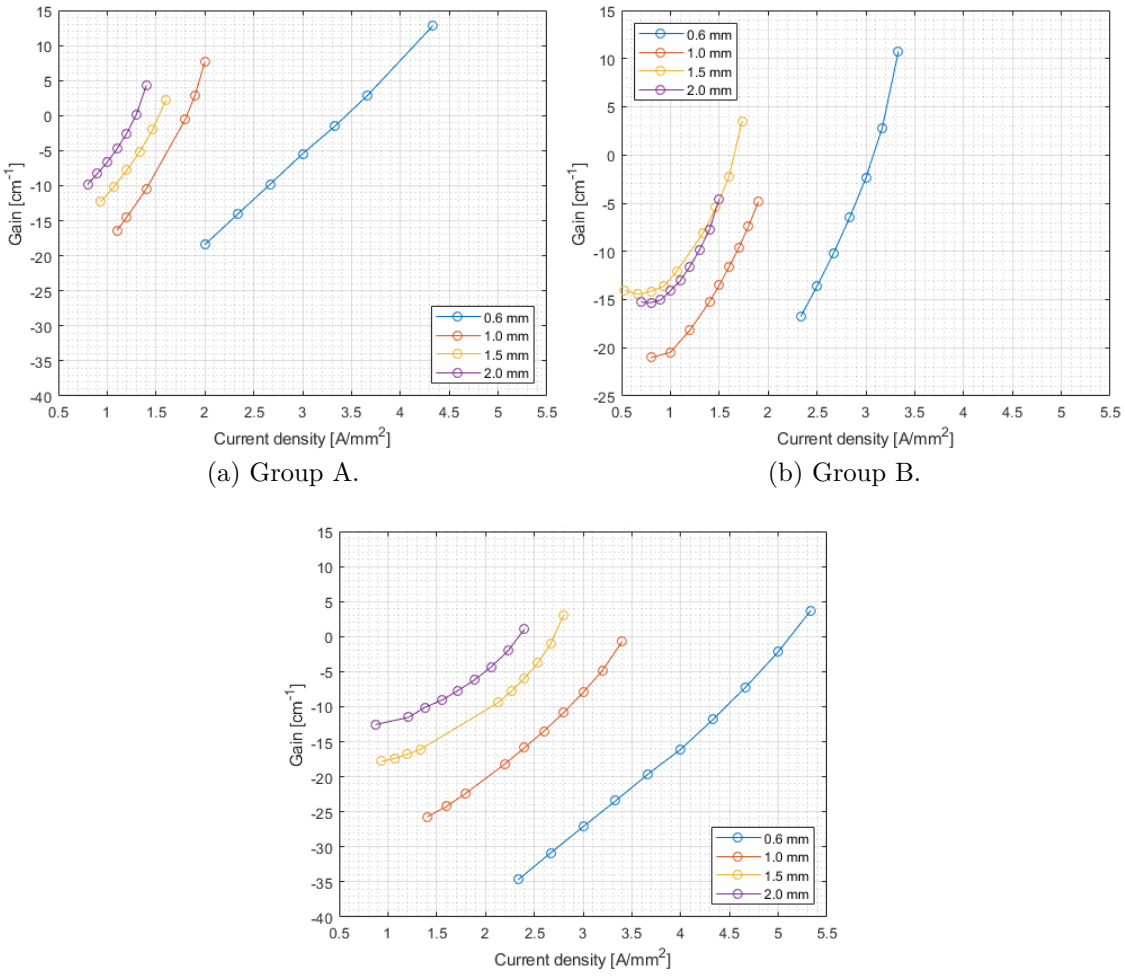

(a) Group A.

(b) Group B.

(c) Group C.

Figure A.9: Maximum net modal gain as function of injection current, by doping level.

A.5 Wavelength shift

A.5.1 Active region length modulation

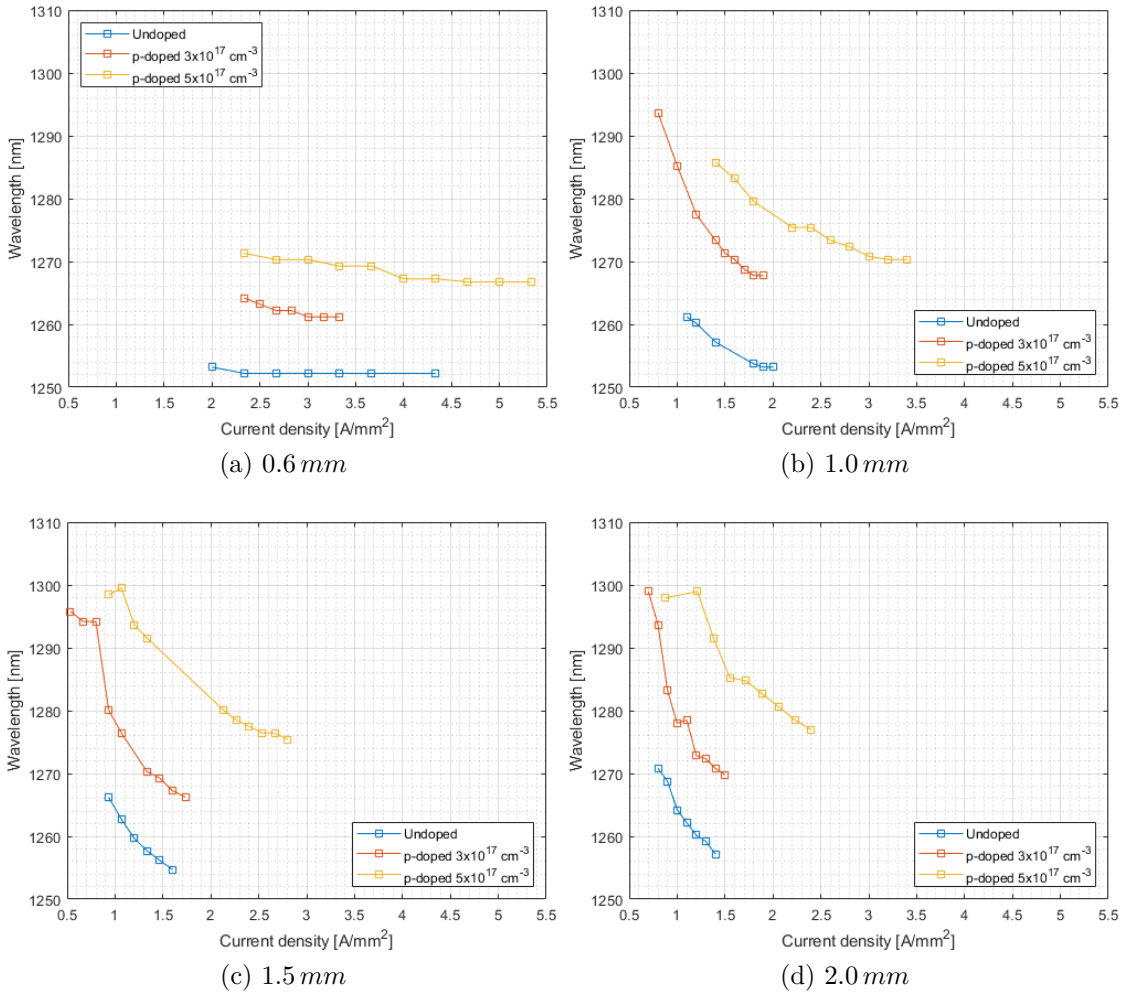

(a) 0.6 mm (b) 1.0 mm

(c) 1.5 mm (d) 2.0 mm

Figure A.10: Wavelength shift as function of injection current, by active region length.

A.5.2 Doping level modulation

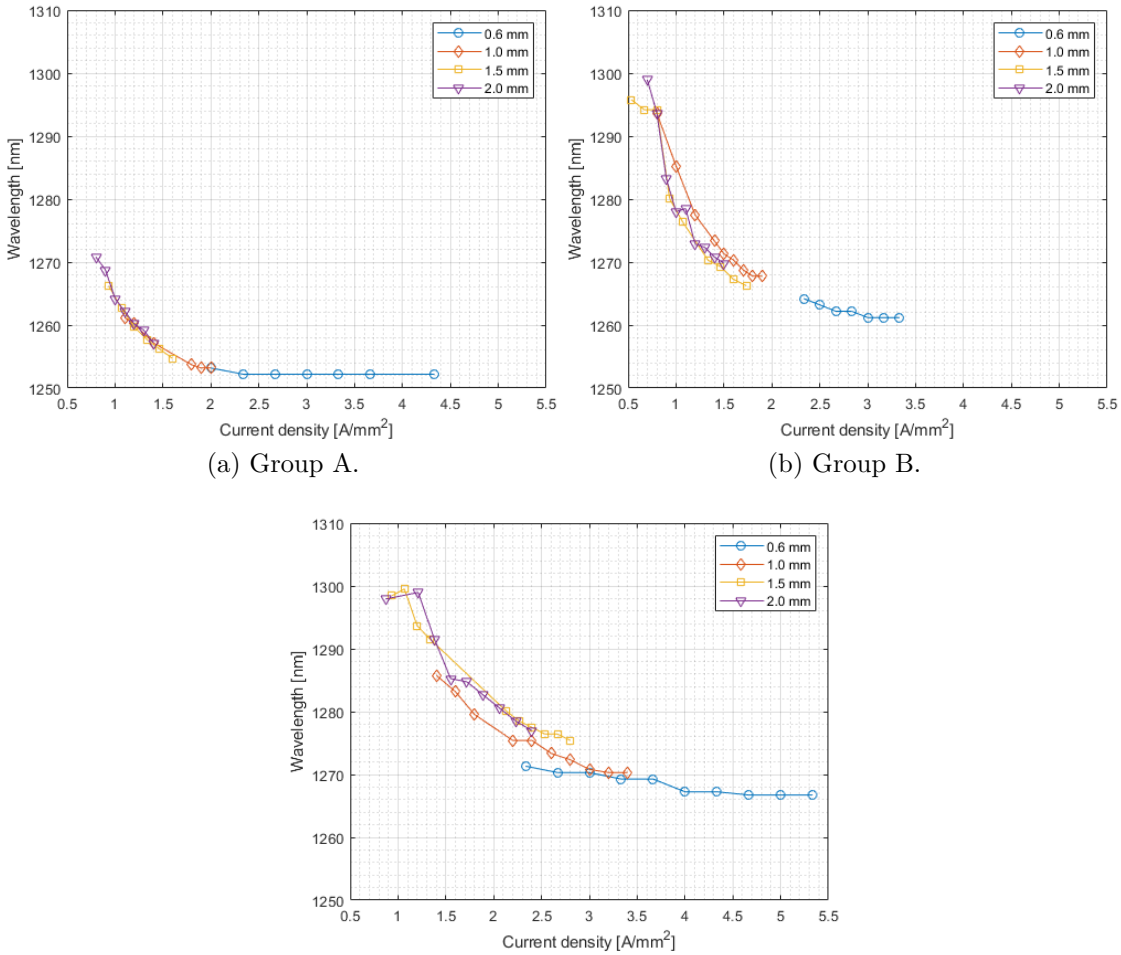

(a) Group A.

(b) Group B.

(c) Group C.

Figure A.11: Wavelength shift as function of injection current, by doping level.

A.6 Group Delay Dispersion

A.6.1 Group A

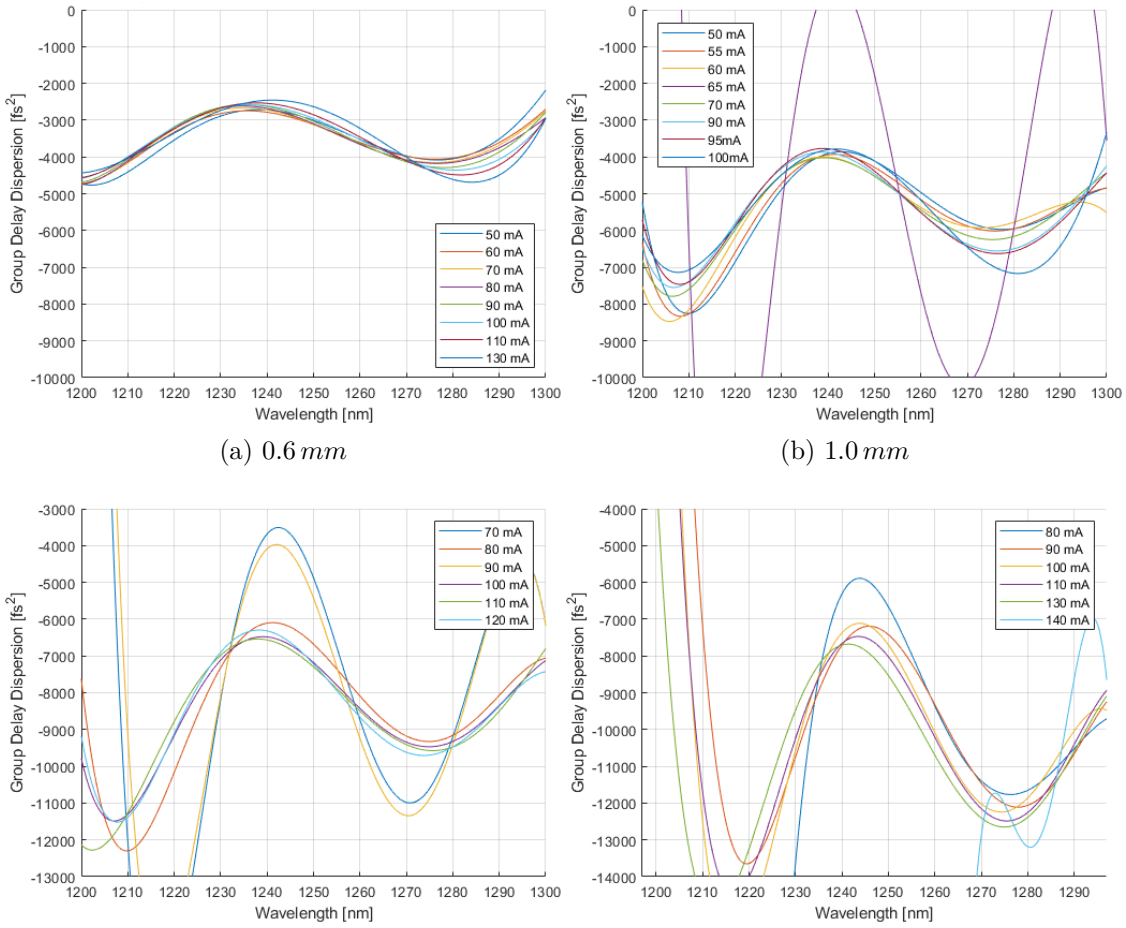

(a) 0.6 mm (b) 1.0 mm

(c) 1.5 mm (d) 2.0 mm

Figure A.12: Group delay dispersion for the undoped devices.

A.6.2 Group B

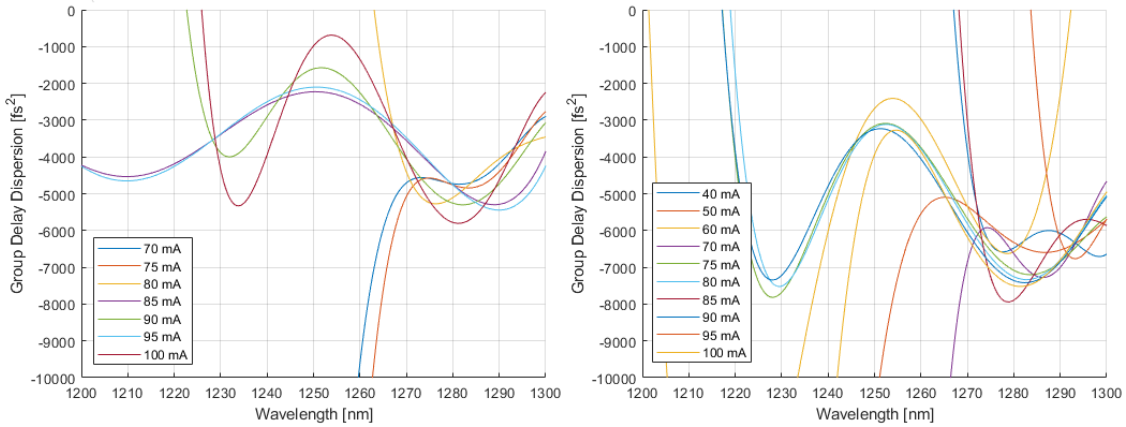

(a) 0.6 mm

(b) 1.0 mm

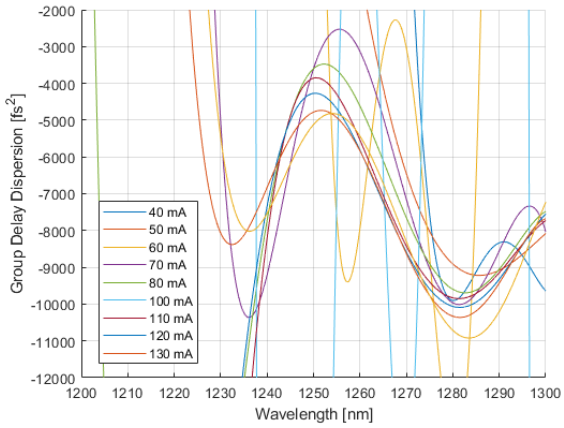

(c) 1.5 mm

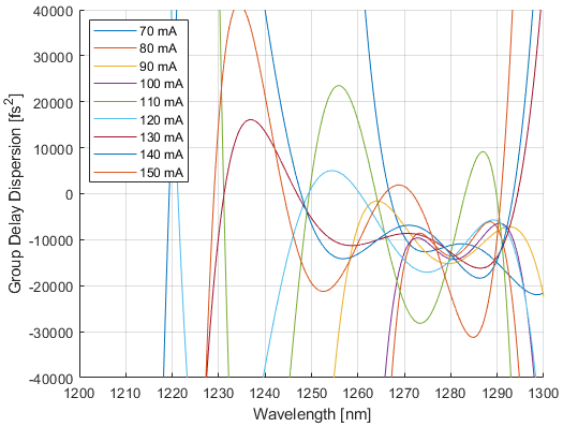

(d) 2.0 mm

Figure A.13: Group delay dispersion for the 3×10^{17} cm^{-3} doped devices.

A.6.3 Group C

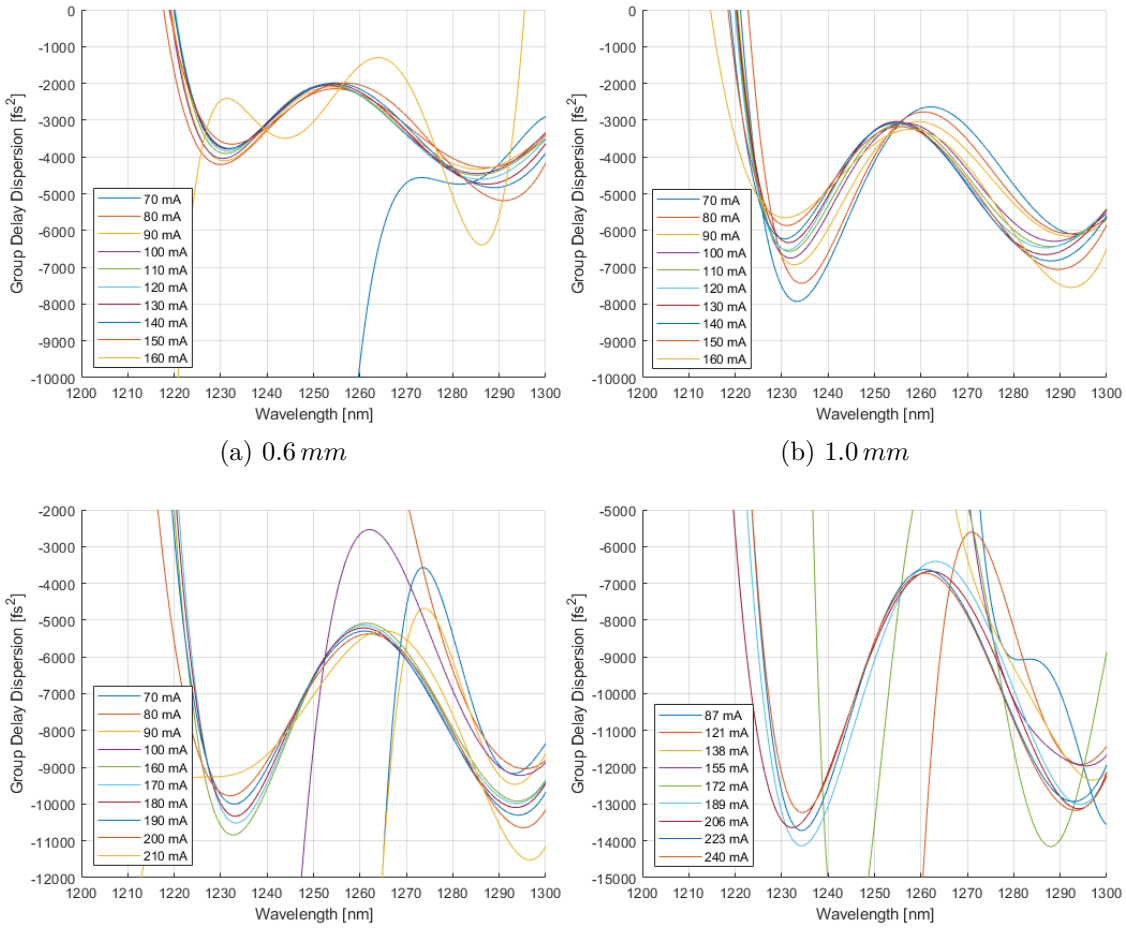

(a) 0.6 mm (b) 1.0 mm

(c) 1.5 mm (d) 2.0 mm

Figure A.14: Group delay dispersion for the 5×10^{17} cm^{-3} doped devices.

A.7 Temperature dependence

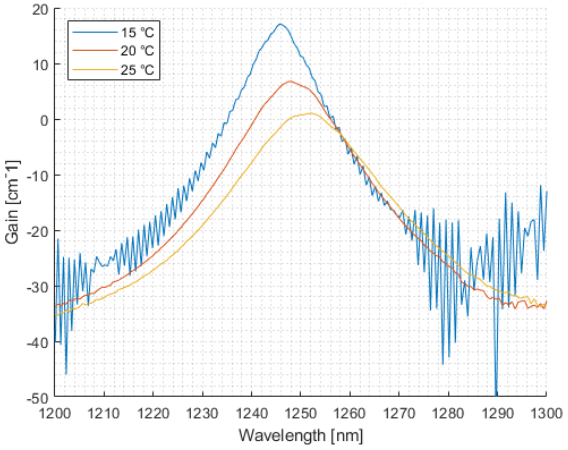

(a) Undoped device, 0.6 *mm*.

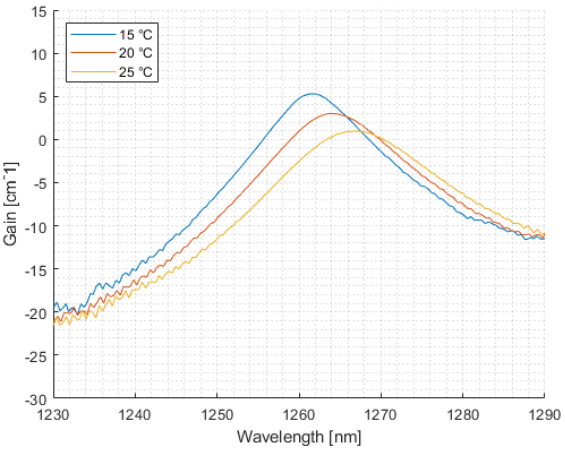

(b) Group B device, 1.5 *mm*.

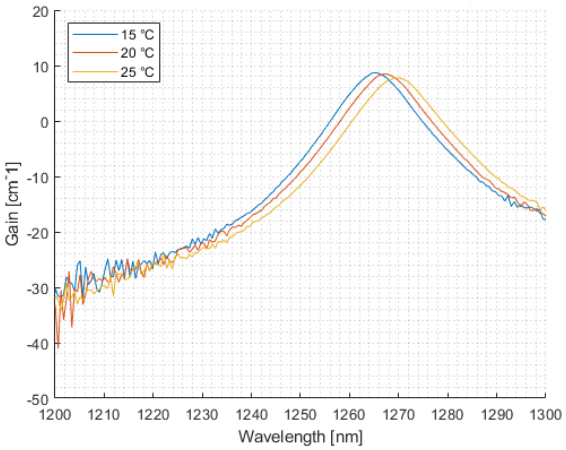

(c) Group C device, 1 *mm*.

Figure A.15: Temperature behaviour of different devices for injection current slightly below threshold.

Appendix B

Post-process Script

B.1 Hakki-Paoli method

```
%% HAKKI-PAOLI METHOD FOR THE GAIN SPECTRA EVALUATION

%% Load the ASE spectra and set constants

[Files, Value]=GetMatchingFiles('*mA.0_spec');

R=0.32;                         % Reflectivity
L=600e-4;                       % Length [cm]
W=50e-4;                        % Width [cm]
max_wavelength=1300;            % [nm]
min_wavelength=1200;            % [nm]
J=Value/(L*W)*1e-5;             % [A/mm^2]

FSR=0.30;                       % Free Spectral Range

%% Main algorithm for reading, processing and plotting

figure;
for k=1:length(Files)

    A=readmatrix(Files{k},'FileType','text');
    Y=A(:,2);
    if A(1,1)<5000
        X=A(:,1);
    else
        X=1./A(:,1)*1e7;
    end

    valley(1)=Y(1);
    pos(1)=X(1);
    index(1)=1;

    t=2;

    for i=2:length(Y)-1

        if Y(i)<=Y(i+1) && Y(i)<=Y(i-1)

            valley(t)=Y(i);
            pos(t)=X(i);
```

```
41
42                  if abs(pos(t)-pos(t-1))>0.3
43
44                      index(t)=find(X==pos(t));
45
46                      Imax(t-1)=max(Y([index(t-1):index(t)]));
47                      Imin(t-1)=min(Y([index(t-1):index(t)]));
48
49                      r(t-1)=Imax(t-1)/Imin(t-1);
50
51                      g(t-1)=1/L*log((sqrt(r(t-1))-1)/(sqrt(r(t
                            -1))+1))+1/(2*L)*log(1/R^2);
52                      wavel(t-1)=max(X([index(t-1):index(t)]));
53
54                      deltawavel=abs(pos(t)-pos(t-1))*10e-9;
55                      n_vect(t-1)=(wavel(t-1)*10e-9)^2/(2*L*10e
                            -2*deltawavel);
56
57                      t=t+1;
58                  end
59              end
60          end
61
62          a=min(find(wavel<1270));
63          b=max(find(wavel>1250));
64          max_g(k)=max(g([a:b]));
65          max_w(k)=wavel(find(g([a:b])==max_g(k)));
66          n=sum(n_vect)/t;
67
68          hold on;
69          hLine=plot(wavel,g,'displayname',sprintf('%.2f A/mm^2',
                J(k)));
70
71      end
72      legend('show','Location','NorthWest');
73      xlim([1200 1300]);
74      ylim([-50 20])
75      grid minor
76      xlabel('Wavelength [nm]')
77      ylabel('Gain [cm^-1]')
78      title('Modal gain spectra')
```

B.2 Mode-Sum method

```
%% MODE-SUM METHOD FOR THE GAIN SPECTRA EVALUATION

%% Load the ASE spectra and set constants

[Files, Value]=GetMatchingFiles('*mA.txt');

R=0.32;                         % Reflectivity
L=1000e-4;                      % Length [cm]
W=50e-4;                        % Width [cm]
max_wavelength=1300;            % [nm]
min_wavelength=1200;            % [nm]
J=Value/(L*W)*1e-5;             % [A/mm^2]

FSR=0.18;                       % Free Spectral Range

%% Main algorithm for reading, processing and plotting

figure;
for k=1:length(Files)

    A=readmatrix(Files{k},'FileType','text');
    Y=A(:,2);
    if A(1,1)<5000
        X=A(:,1);
    else
        X=1./A(:,1)*1e7;
    end

    valley(1)=Y(1);
    pos(1)=X(1);
    index(1)=1;

    t=2;

    for i=2:length(Y)-1

        if Y(i)<=Y(i+1) && Y(i)<=Y(i-1)

            valley(t)=Y(i);
            pos(t)=X(i);
```

```
41
42                  if abs(pos(t)-pos(t-1))>0.3
43
44                      index(t)=find(X==pos(t));
45
46                      area(t-1)=trapz(X([index(t-1):index(t)]),Y
                            ([index(t-1):index(t)]));
47                      Imin(t-1)=min(Y([index(t-1):index(t)]));
48                      delta(t-1)=X(index(t))-X(index(t-1));
49
50                      y(t-1)=area(t-1)/(Imin(t-1)*delta(t-1));
51
52                      g(t-1)=1/L*log((y(t-1)-1)/(y(t-1)+1))-1/L*
                            log(R);
53                      wavel(t-1)=max(X([index(t-1):index(t)]));
54
55                      deltawavel=abs(pos(t)-pos(t-1))*10e-9;
56
57                      t=t+1;
58                  end
59              end
60          end
61
62          a=min(find(wavel<1270));
63          b=max(find(wavel>1250));
64          max_g(k)=max(g([a:b]));
65          wavel_cut=wavel([a:b]);
66          max_w(k)=wavel_cut(find(g([a:b])==max_g(k)));
67          n=sum(n_vect)/t;
68
69          hold on;
70          hLine=plot(wavel,g,'displayname',sprintf('%.2f A/mm^2',
                J(k)));
71
72      end
73      legend('show','Location','NorthWest');
74      xlim([1230 1290]);
75      ylim([-30 15])
76      grid minor
77      xlabel('Wavelength [nm]')
78      ylabel('Gain [cm^-1]')
79      title('Modal gain spectra')
```

B.3 FTIR

```
%% FTIR FOR THE GAIN SPECTRA EVALUATION

%% Load interferograms and set constants

[Files, Value]=GetMatchingFiles('*mA_C1.0mm_25grad_20scans.0_ifg');

R=0.32;                         % Reflectivity
L=1000e-4;                      % Length [cm]
W=50e-4;                        % Width [cm]
max_wavelength=1300;            % [nm]
min_wavelength=1200;            % [nm]
J=Value/(L*W)*1e-5;             % [A/mm^2]

N=5000;                         % N of points around harmonic peaks
HeNe=632.8/2;                   % Half of the interf. laser wavelength

%% Main algorithm for reading, processing and plotting

figure;
for k=1:length(Files)
    ifg=readmatrix(Files{k},'FileType','text');
    Y=ifg(2:ceil(end/4),2);
    X=ifg(2:ceil(end/4),1);
    Xscaled=ifg(2:ceil(end/4),1)*HeNe*10^-7;
    MathMax = 1/(HeNe);   % scaling factor for the x-axis (half of the interferometer laser wavelength)
    ink = MathMax/(2*N+1);
    f=1./(ink:ink:MathMax-ink);
    index_i=max(find(f>max_wavelength));
    index_f=min(find(f<min_wavelength));
    [Max0, H0]=max(Y);
    Thr=10;
    while Thr<10000
        H1=find(Y(H0+N:end-N)>Max0/Thr,1);
        if isempty(H1)
            Thr=Thr+10;
        else
```

```
37                  break;
38              end
39          end
40          if Thr==10000
41              continue;
42          end
43          H1=H1+H0+N-1;
44          [Max1, H1Tmp]=max(Y(H1-N:H1+N-1));
45
46          H1=H1-1+H1Tmp-N;
47          [Max0, H0]=max(Y);
48
49          PtNum=H1-N:H1+N-1;
50          PtDen=H0-N:H0+N-1;
51
52          W1=Y(PtNum);
53          W2=Y(PtDen);
54
55          Num=ifft(W1);
56          Den=ifft(W2);
57
58          b=abs(Num./Den);
59          phi=angle(Num);
60          ac=abs(Num);
61
62          g=1/L*log(b/R);
63
64          max_g(k)=max(g([index_i:index_f]));
65          max_w(k)=f(index_i+find(g([index_i:index_f])==max_g(k))
                );
66
67          hold on;
68          hLine=plot(f,g,'displayname',sprintf('%.2f A/mm^2',J(k)
                ));
69  end
70  legend('show','Location','NorthWest');
71  xlim([1200 1300]);
72  ylim([-50,20])
73  grid minor
74  xlabel('Wavelength [nm]')
75  ylabel('Gain [cm^-1]')
76  title('Modal gain spectra FTIR')
```

Bibliography

[1] T. H. Maiman, *Stimulated optical radiation in ruby*, Nature **187**, 493, 1960.

[2] R. Dupuis, *An introduction to the development of the semiconductor laser*, Journal of Quantum Electronics, **23**, 651, 1987.

[3] R. J. Keyes, T. M. Quist, *Recombination radiation emitted by gallium arsenide*, Proc. IRE **50**, 1822, 1962.

[4] I. Hayashi et al. *Junction lasers which operate continuously at room temperature*, Applied Physic Letters, **17**, 109, 1970.

[5] D. Huffaker et al. *Continuous wave low-threshold performance of* 1.3 μm *InGaAs-GaAs quantum-dot lasers.* IEEE JSTQE, **6**, 452, 2000.

[6] K. Mukai et al. *High characteristic temperature of near*-1.3 μm *InGaAs/GaAs quantum dot laser at room temperature.* Applied Physics Letters, **76**, 3349, 2000.

[7] S. Franchi et al. *Quantum dot nanostructures and molecular beam epitaxy.* Progress in Crystal Growth and Characterization of Materials, **47**, 166, 2003.

[8] M. Sugawara *Self assembled InGaAs/GaAs quantum dots.* Semiconductor and semimetals, Academic Press, 1999.

[9] A. Wojs et al. *Electronic structure and magneto-optics of self-assembled quantum dots.* Physical Review B, **54**, 5604, 1996.

[10] J. Kim et al. *Static gain saturation model of quantum-dot semiconductor optical amplifiers.* IEEE Journal of Quantum Electronics **44**, 658, 2008.

[11] J. Kim et al. *Numerical simulation of temporal and spectral variation of gain and phase recovery in quantum dot semiconductor optical amplifiers.* IEEE Journal of Quantum Electronics **46**, 405, 2010.

[12] C. Tong *Rate equations for* 1.3 μm *dots-under-a-well and dots-in-a-well self-assembled InAs/GaAs quantum-dot lasers.* IEEE Journal of Quantum Electronics **42**, 1175, 2006.

[13] M. Gioannini et al. *Simulations of differential gain and linewidth enhancement factor of quantum dot semiconductor lasers*, Optical and Quantum Electronics, **38**, 381, 2006.

[14] P. Griffiths et al. *Fourier Transform Infrared Spectrometry.* Wiley-Blackwell, 2^{nd} edition, ISBN 978-0-471-19404-0, 2007,

[15] H. Shams, et alt. *Photonic generation for multichannel THz wireless communication*, Optics Express, **22**(19), 2014.

[16] D. Auth, C. Weber et al. *Emission dynamics of monolithic broad-area InAs/InGaAs quantum dot lassers*, poster number HL 35.70, DPG Regensburg, 2019.

[17] D. Auth, C. Weber et al. *Modal gain and dispersion of monolithic broad-area InAs/InGaAs quantum dot lasers*, poster number HL 35.71, DPG Regensburg, 2019.

[18] M. Angelozzi et al. *Modal gain, dispersion, and line-width enhancement factor of quantum-dot laser*, SPIE Photonics West 2020, paper 11301-67,.

[19] Z. Zhang et al. *Effects of modulation p doping in InAs quantum dot lasers on silicon*, Applied Physics Letters **113**, 061105, 2018.

[20] P. M. Smowton et al. *Gain in p-doped quantum dot lasers*, Journal of Applied Physiscs, **101**, 013107, 2007.

[21] S. S. Konoplev et al. *Modulation doping of quantum dot laser active area and its impact on lasing performance*, Journal of Physics, **642**, 012039, 2015.

[22] B. W. Hakki, T. L. Paoli *Gain spectra in GaAs double-heterostructure injection lasers*, Journal of Applied Physics, **46**, 1299, 1975.

[23] D. T. Cassidy *Technique for measurement of the gain spectra of semiconductor diode lasers*, Journal of Applied Physics, **56**, 3096, 1984.

[24] G. E. Shtengel et al. *Advances in measurements of physical parameters of semiconductor lasers*, IJHSES, **9**, 901, 1998.

[25] D. Hofstetter, J. Faist *Measurement of Semiconductor Laser Gain and Dispersion Curves Utilizing Fourier Transforms of the Emission Spectra*, Photonics Technology Letters, **11**, 1372, 1999.

[26] G. Ozgur et al. *Threshold temperature dependence of a Quantum Dot laser diode with and without p-doping.*, Journal of Quantum Electronics, **45**, 1265, 2009.

[27] J. Mukherjee et al. *Spatial mode dynamics in wide-aperture quantum-dot lasers*, Physical Review A, **79**, 053813, 2009.

[28] T. C. Newell et al. *Gain and linewidth enhancement factor in InAs Quantum-Dot laser diodes*, IEEE Photonics Technology Letters, **11**, 1527, 1999.

[29] D. Rodriguez et al. *Gain, Index Variation, and Linewidth-Enhancement Factor in 980-nm Quantum-Well and Quantum-Dot Lasers*, Journal of Quantum Electronics, **41**, 117, 2005.

[30] D. Rodriguez et al. *Measurement of gain spectra, refractive index shift and linewidth enhancement factor in Al-free 980 nm lasers with broadened waveguide.* Proceedings of SPIE, **4646**, 344, 2002.

[31] D. J. Bossert, D. Gallant, *Gain, Refractive Index, and α Parameter in InGaAs GaAs SQW Broad Area Lasers*, Photonics Technology Letters, **8**, 322, 1996.

[32] C. Wang et al. *Thermally insensitive determination of the linewidth broadening factor in nanostructured semiconductor lasers using optical injection locking*, Scientific Report, **6**, 27285, 2016.

[33] F. I. Zubov et al. *Observation of zero linewidth enhancement factor at excited state band in quantum dot laser*, Electronic Letters, **51**, 1686, 2015.

[34] A. Martinez et al. *Static and dynamic measurements of the α factor of five quantum dot layer single mode lasers emitting at 1.3 μm on GaAs*, Applied Physics Letters, **86**, 211115, 2005.